

ARTICLE TYPE

Coupling fully resolved light particles with the Lattice Boltzmann method on adaptively refined grids

Lukas Werner*¹ | Christoph Rettinger¹ | Ulrich Rüde^{1,2}¹Chair for System Simulation, Friedrich–Alexander–Universität Erlangen–Nürnberg, Cauerstraße 11, 91058 Erlangen, Germany²CERFACS, 42 Avenue Gaspard Coriolis, 31057 Toulouse Cedex 1, France**Correspondence**

*Lukas Werner, Cauerstraße 11, 91058 Erlangen, Email: lks.werner@fau.de

Present Address

Chair for System Simulation, Friedrich–Alexander–Universität Erlangen–Nürnberg, Cauerstraße 11, 91058 Erlangen, Germany

Abstract

The simulation of geometrically resolved rigid particles in a fluid relies on coupling algorithms to transfer momentum both ways between the particles and the fluid. In this article, the fluid flow is modeled with a parallel Lattice Boltzmann method using adaptive grid refinement to improve numerical efficiency. The coupling with the particles is realized with the momentum exchange method. When implemented in plain form, instabilities may arise in the coupling when the particles are lighter than the fluid. The algorithm can be stabilized with a virtual mass correction specifically developed for the Lattice Boltzmann method. The method is analyzed for a wide set of physically relevant regimes, varying independently the body-to-fluid density ratio and the relative magnitude of inertial and viscous effects. These studies of a single rising particle exhibit periodic regimes of particle motion as well as chaotic behavior, as previously reported in the literature. The new method is carefully compared with available experimental and numerical results. This serves to validate the presented new coupled Lattice Boltzmann method and additionally it leads to new physical insight for some of the parameter settings.

KEYWORDS:

Lattice Boltzmann Method; Direct Numerical Simulation; Adaptive Grid Refinement; Explicit Coupling; Light Sphere

1 | INTRODUCTION

Light particles, here understood as particles with a solid-to-fluid density ratio $\pi_p = \rho_p/\rho_f < 1$, appear in various applications and situations. During ascension in an otherwise resting fluid they exhibit a multitude of movement patterns often strongly deviating from straight paths. This depends on shape, density ratio, and surrounding fluid properties. As a matter of fact, strictly straight paths only occur in a comparatively small parameter range. This makes way to consider the implications of such non-regular paths in practical settings. As an environmental problem, floatsam in the form of microplastics with a density slightly lower than water may harm the biosphere in oceans^{1,2,3} and lakes⁴. Here the density ratio ranges from $\pi_p \approx 0.9$ for polypropylene to $\pi_p \approx 0.01$ in the case of expanded polystyrene⁴. Furthermore, in a natural setting, rising bubbles and particles in oceans support the formation of warmer regions with stronger temperature gradients^{5,6}. Facilitating the dispersion of fluid and matter, the turbulent structures induced by moving bubbles of low density ratios in a mixture is also of interest in engineering applications^{7,8,9}. Two examples are fuel sprays in combustion engines and bubbly flows in industrial reaction catalysis^{10,11}. In aerodynamics the effects are observed for meteorology balloons^{12,13}, and in the context of autorotation of individual objects¹⁴.

Above examples typically involve a huge number of particles, whereas even the movement of a single spherical particle exhibits complex behaviors. A light, spherical body submerged in water under the sole influence of gravity may either rise in a straight line, move obliquely, enter a regular or rather chaotic zig-zagging movement. As reported by Jenny *et al.*¹⁵, this depends on the density ratio π_p and the Galileo number Ga , which describes the ratio between buoyant and viscous forces. They used numerical simulation to study the particle paths, varying these two parameters. In the following, Veldhuis & Biesheuvel¹⁶, Horowitz & Williamson¹⁷ and Ostmann, Chaves & Brucker¹⁸, among others, performed laboratory experiments to obtain physical comparison results. To address the found contradictions, Zhou & Dušek¹⁹ and Auguste & Magnaudet²⁰ performed an extensive set of detailed numerical simulations. Albeit very efficient for such specific setups, these recent simulation approaches are usually not extensible to multiple particles or arbitrary domains due to the usage of spectral methods, making them only suitable for a single freely moving sphere.

Such restrictions are not present for other methods in computational fluid dynamics (CFD), such as finite volume methods^{21,22} or the lattice Boltzmann method^{23,24} (LBM). Many of the previously mentioned scenarios involving bubbly flows can be approximated by modeling those submerged small bubbles as rigid spheres in a fluid due to their low Eötvös number²⁵. This enables the usage of a Lagrangian description for the solid phase by employing discrete particle simulation. In combination with fluid-particle coupling that enables geometrically fully resolved simulations of the flow around the particle and the fluid-solid interactions, predictive studies of a large variety of particulate systems become possible^{26,27,28,29}. In this work, we focus on the LBM which is a relatively recent Eulerian computational method to simulate fluids. The LBM is well suited for large scale simulations and massively parallel execution^{30,31,32}.

The fully coupled interaction between the solid Lagrangian and the fluid Eulerian phase is achieved by the momentum exchange method (*MEM-LBM*)^{33,34,35}. However, the *MEM-LBM* on its own is only partially applicable for simulations of light particles, as intended in the present work. It is known to suffer from instabilities when density ratios approach zero. The stability condition of the original coupling by Ladd *et al.*³⁶ was given as $\pi_p d_p / \Delta x > 20$, where $d_p / \Delta x$ is the numerical resolution in terms of cells per particle diameter. With the improvements by Aidun *et al.*³⁴, density ratios close to one could be realized.

This issue of numerical instability at those circumstances is not restricted to the *MEM-LBM* and reported for many CFD methods that apply an explicit fluid-particle coupling. For the popular immersed boundary method³⁷ (IBM), e.g., the lower bound initially resided at $\pi_p = 1.2$. Improvements to the imposition of boundary conditions on the interface and an additional integration step for the artificial flow field inside the particles allowed stable results at $\pi_p > 0.3$ ^{38,39}. To gain a fully stable solution at arbitrary density ratios, much more costly implicit schemes were proposed^{40,41,42}.

The reason for the instabilities in explicit coupling schemes is attributed to the particles' mass being exceeded by its so-called added mass, i.e. the fluid attached to the moving particle. In an explicit coupling scenario, this mass cannot be properly accounted for, which results in excessive accelerations on startup that lead to oscillations^{43,44}. In an effort to stabilize explicit schemes at density ratios as low as $\pi_p = 0.001$, Schwarz *et al.* investigated the cause of stability issues in the IBM⁴⁵. By introducing an auxiliary virtual force and a virtually increased mass of purely numerical nature to the particle, stable simulations of light particles could be obtained. This scheme was termed the "virtual mass approach" by the authors.

In this paper, we aim to improve the existing *MEM-LBM* and extend it to simulations of particles with very low density ratios. To this end, we follow and improve the approach by Schwarz *et al.*, resulting in a *MEM-LBM* enhanced by virtual mass (*VM-MEM-LBM*). This will allow for predictive numerical studies of such setups. As an illustrative example and to demonstrate the applicability of our approach, we investigate the movement of a single rising sphere in an unbounded domain. In an effort to validate existing results from literature, demonstrate the capabilities of the *VM-MEM-LBM* and enabling a scalable simulation of submerged light spheres, we apply the LBM to this problem. To our best knowledge, our article is the first to apply the LBM in a wide range of parameter settings of this situation.

Improving the efficiency of these simulations, an adaptive grid refinement technique is employed. Since domains with a height in the order of 100 times of the sphere diameter are necessary, many regions of the fluid remain stale during the motion of the sphere, requiring only coarse resolutions. On the other hand, increasing turbulences and strong velocity gradients especially at the fluid-solid interface require a high resolution to yield satisfying results. Thus, a grid, which locally adapts its spacing, is desirable.

The paper is structured as follows. In Section 2, the *MEM-LBM* as used for the simulations throughout this paper is outlined. Section 3 starts with a numerical study to investigate and discuss the lower density ratio limits of the *MEM-LBM*. Next, this method is enhanced by the virtual mass approach, resulting in the *VM-MEM-LBM*. Efficiency improvements by employing adaptive grid refinement and criteria for determining the need of a change in resolution are explained in Section 4. Section 5

presents an extensive study of the movement trajectories and vortices of rising spheres to demonstrate the practical use of *MEM-LBM* and *VM-MEM-LBM*. We conclude with a summary in Section 6.

2 | NUMERICAL METHOD

The here employed CFD method is based on the recently developed approach presented and validated in Ref. 46. For completeness, we outline the main aspects of the fluid flow simulation and the fluid-particle coupling in the following and refer to this work for a more detailed description. All presented methods can be found in the open-source repository¹ of the WALBERLA framework³².

2.1 | Lattice Boltzmann Method

The lattice Boltzmann method (LBM) is based on an Eulerian representation of the fluid field by mesoscopic kinetic equations, that fulfill the macroscopic Navier-Stokes equations^{23,47}. It computes the temporal evolution of particle distribution functions (PDFs) f_q in the cells of a Cartesian lattice using a discrete solution of the Boltzmann equation. The LBM is commonly described using the $DdQq$ notation with d spatial dimensions and q discrete velocities \mathbf{c}_q ⁴⁸. A common choice for three dimensional simulations is D3Q19 which will be employed throughout this paper.

Being an explicit numerical scheme in time, the equation to advance the PDFs of a cell \mathbf{x} by one time step of size Δt is given by

$$f_q(\mathbf{x} + \mathbf{c}_q \Delta t, t + \Delta t) = \tilde{f}_q(\mathbf{x}, t) = f_q(\mathbf{x}, t) - C_q(f_1(\mathbf{x}, t), \dots, f_{19}(\mathbf{x}, t)), \quad (1)$$

where C corresponds to a general collision operator. It is applied during the collision step, i.e. the right part of the equation, to update the local PDFs in each cell \mathbf{x} inside the domain. The left part denotes the streaming step of the LBM, which constitutes distribution of the post-collision PDFs $\tilde{f}_q(\mathbf{x}, t)$ to the neighboring cells.

The local macroscopic fluid density ρ_f and velocity \mathbf{u}_f are given as moments of the distribution functions²³:

$$\rho_f(\mathbf{x}, t) = \sum_q f_q(\mathbf{x}, t), \quad \rho_0 \mathbf{u}_f(\mathbf{x}, t) = \sum_q f_q(\mathbf{x}, t) \mathbf{c}_q, \quad (2)$$

where ρ_0 is a constant average density, that is introduced to reduce inherent compressibility effects⁴⁹.

In LBM, quantities are commonly formulated in so-called lattice units, such that the cell size $\Delta x = 1$, time step size $\Delta t = 1$ and $\rho_0 = 1$.

In the multiple-relaxation-time (MRT) formulation, the collision operator C is written using a diagonal relaxation matrix \mathbf{S} , containing the relaxation factors, and a corresponding matrix \mathbf{M} , which linearly transforms the distribution functions to the moment space, where the collision is carried out⁵⁰. The collision operator is thus given as

$$C = \mathbf{M}^{-1} \mathbf{S} \mathbf{M}. \quad (3)$$

In particular, we here employ the specific MRT model from Ref. 46, which uses the transformation matrix \mathbf{M} given in Ref. 51 and the relaxation matrix

$$\mathbf{S} = \text{diag}(0, 0, 0, 0, s_b, s_b, s_v^-, s_v^-, s_v^-, s_v, s_v, s_v, s_v, s_v, s_v, s_v, s_v, s_v^-, s_v^-, s_v^-). \quad (4)$$

Via its three parameters, it allows for explicit control over the kinematic fluid viscosity ν_f and the bulk viscosity ν_b , given as

$$\nu_f = c_s^2 \Delta t \left(\frac{1}{s_v} - \frac{1}{2} \right), \quad \nu_b = \frac{2}{3} c_s^2 \Delta t \left(\frac{1}{s_b} - \frac{1}{2} \right), \quad (5)$$

with the lattice speed of sound c_s , and provides an accurate representation of boundaries⁴⁶. Parameterization can conveniently be done by introducing the so-called “magic” parameter Λ ⁵², which we set to $3/16$, and a bulk factor Λ_b ⁵³

$$\Lambda = \left(\frac{1}{s_v} - \frac{1}{2} \right) \left(\frac{1}{s_v^-} - \frac{1}{2} \right), \quad \Lambda_b = \frac{\left(\frac{1}{s_b} - \frac{1}{2} \right)}{\left(\frac{1}{s_v} - \frac{1}{2} \right)}. \quad (6)$$

Choosing $\Lambda_b = 1$ results in the two-relaxation-time (TRT) collision operator⁵². Unless stated otherwise, we employ $\Lambda_b = 100$.

¹www.walberla.net

Throughout the paper, we consistently make use of the commonly applied lattice unit system, given by the cell size $\Delta x = 1$, the time step size $\Delta t = 1$, $c_s = 1/\sqrt{3}$, and $\rho_0 = 1$.

2.2 | Rigid Particle Motion

The Lagrangian dynamics of a spherical rigid particle is governed by the temporal evolution of its position \mathbf{x}_p , translational velocity \mathbf{u}_p and angular velocity $\boldsymbol{\omega}_p$, and is described by

$$\frac{d\mathbf{x}_p}{dt} = \mathbf{u}_p, \quad (7a)$$

$$m_p \frac{d\mathbf{u}_p}{dt} = \mathbf{F}_p, \quad (7b)$$

$$I_p \frac{d\boldsymbol{\omega}_p}{dt} = \mathbf{T}_p, \quad (7c)$$

where $m_p = \rho_p V_p$ is the particle's mass, with the particle density ρ_p and its volume V_p , and I_p corresponds to its moment of inertia. Gravitation and buoyancy contributions are given as $\mathbf{F}_p^g = (\rho_p - \rho_f) \mathbf{g} V_p$, with the gravitational acceleration \mathbf{g} . Together with the fluid-particle interaction force \mathbf{F}_p^{hyd} , they are the total force acting on the particle, $\mathbf{F}_p = \mathbf{F}_p^g + \mathbf{F}_p^{hyd}$. Accordingly, the particle's torque is $\mathbf{T}_p = \mathbf{T}_p^{hyd}$.

Temporal integration of Equations (7a) to (7c) is achieved by explicit time stepping using a Velocity-Verlet scheme. The explicit update formulas are expressed as^{54,46}

$$\mathbf{x}_p(t + \Delta t) = \mathbf{x}_p(t) + \Delta t \mathbf{u}_p(t) + \frac{\Delta t^2}{2m_p} \mathbf{F}_p(t), \quad (8a)$$

$$\mathbf{u}_p(t + \Delta t) = \mathbf{u}_p(t) + \frac{\Delta t}{2m_p} (\mathbf{F}_p(t) + \mathbf{F}_p(t + \Delta t)), \quad (8b)$$

$$\boldsymbol{\omega}_p(t + \Delta t) = \boldsymbol{\omega}_p(t) + \frac{\Delta t}{2I_p} (\mathbf{T}_p(t) + \mathbf{T}_p(t + \Delta t)). \quad (8c)$$

The force $\mathbf{F}_p(t + \Delta t)$ and torque $\mathbf{T}_p(t + \Delta t)$ are computed with the already updated position. Linear acceleration $\mathbf{a}_p(t + \Delta t)$ and angular acceleration $\boldsymbol{\beta}_p(t + \Delta t)$ are directly given via $\mathbf{F}_p(t + \Delta t)$ and $\mathbf{T}_p(t + \Delta t)$ as

$$\mathbf{a}_p(t + \Delta t) = \frac{\mathbf{F}_p(t + \Delta t)}{m_p}, \quad (9a)$$

$$\boldsymbol{\beta}_p(t + \Delta t) = \frac{\mathbf{T}_p(t + \Delta t)}{I_p}. \quad (9b)$$

Rotation is not explicitly accounted for due to the focus on spherical particles. Since inter-particle collisions are not regarded in this work, we do not apply sub-cycling of the particle part and thus make use of the same time step size Δt here as in the LBM⁴⁶.

2.3 | Fluid-Particle Coupling

The coupling between the fluid and solid phase is accomplished via the momentum exchange method (*MEM-LBM*)^{33,34} which has successfully been applied to a variety of particulate flow simulations^{30,35,46}. The core idea lies in differentiating between solid and fluid cells in the discretized computational domain: A particle is mapped into the fluid simulation by marking the cells it occupies as solid, effectively excluding it from the LBM simulation. This mapping has to be continuously updated for moving particles. This allows for a Lagrangian description of the particle, while the properties of the fluid use an Eulerian model.

In this method, the hydrodynamic interaction force is evaluated as the force acting on the surface of the particle. Within the particle only nodes marked as solid are present. Momentum is transferred solely between the particle boundary and the adjacent fluid, as sketched in the left part of Figure 1. Along the fluid-particle boundary, the particle surface velocity acts as a no-slip boundary condition for the fluid. We here employ the higher-order central linear interpolation (CLI) scheme⁵², given by

$$f_{\bar{q}}(\mathbf{x}, t + \Delta t) = \tilde{f}_{\bar{q}}(\mathbf{x}, t) + \kappa_0 \tilde{f}_{\bar{q}}(\mathbf{x} - \mathbf{c}_q \Delta t, t) - \kappa_0 \tilde{f}_{\bar{q}}(\mathbf{x}, t) - 3\alpha \frac{w_q}{c_s^2} \rho_0 \mathbf{v}(\mathbf{x}_b, t) \mathbf{c}_q, \quad (10)$$

with coefficients $\kappa_0 = (1 - 2\delta_q) / (1 + 2\delta_q)$, $\alpha = 4 / (1 + 2\delta_q)$ and where \bar{q} denotes the opposite direction of q . The variable δ_q describes the ratio between the distance from the fluid cell center to the boundary and the distance from the cell center to the

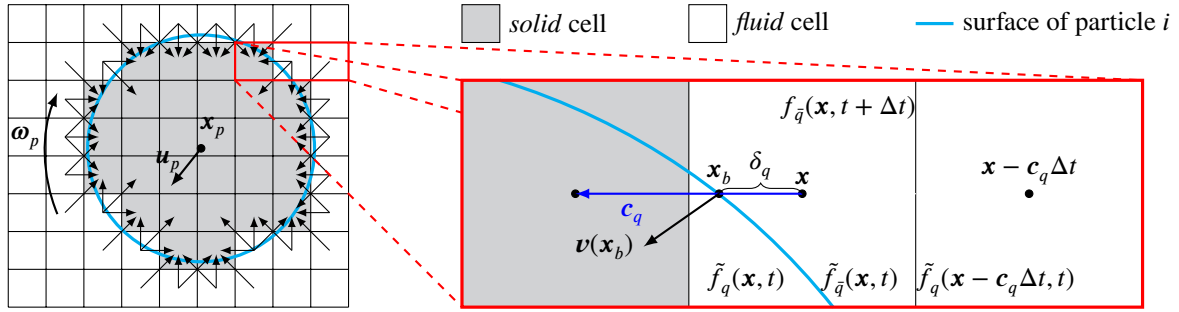


FIGURE 1 Sketch of fluid-particle coupling, including the explicit mapping and the CLI boundary condition.

solid cell center. Therefore, the exact boundary location in direction of the lattice velocity is obtained as $\mathbf{x}_b = \mathbf{x} + \mathbf{c}_q \delta_q$. This introduces subgrid information about the actual boundary location and substantially improves the accuracy to second order, as opposed to the commonly applied simple bounce-back rule that delivers only first order accuracy^{52,35}.

The link-based force contribution $\mathbf{F}_{q_{f-s}}$ acting onto a particle at position \mathbf{x}_b via a fluid-solid link q_{f-s} is given as^{33,55,35}

$$\mathbf{F}_{q_{f-s}}(\mathbf{x}_b, t) = \frac{(\Delta x)^3}{\Delta t} \left((\mathbf{c}_{q_{f-s}} - \mathbf{v}(\mathbf{x}_b, t)) \tilde{f}_{q_{f-s}}(\mathbf{x}, t) - (\mathbf{c}_{q_{f-s}} - \mathbf{v}(\mathbf{x}_b, t + \Delta t)) \tilde{f}_{q_{f-s}}(\mathbf{x}, t + \Delta t) \right). \quad (11)$$

Following Ref. 55, the particle's surface velocity $\mathbf{v}(\mathbf{x}_b, t)$ is subtracted from the lattice velocities to ensure Galilean invariance. Summing up over all contributing nodes q_{f-s} , the total hydrodynamic force \mathbf{F}_p^{hyd} and torque \mathbf{T}_p^{hyd} acting on one submerged particle are obtained:

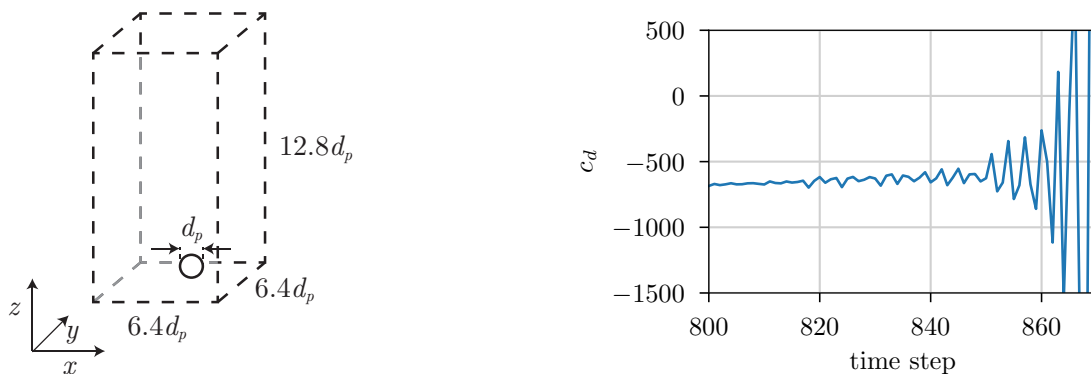
$$\mathbf{F}_p^{hyd} = \sum_{\mathbf{x}_b} \sum_{q_{f-s}} \mathbf{F}_{q_{f-s}}(\mathbf{x}_b, t), \quad \mathbf{T}_p^{hyd} = \sum_{\mathbf{x}_b} \sum_{q_{f-s}} (\mathbf{x}_b - \mathbf{x}_p) \times \mathbf{F}_{q_{f-s}}(\mathbf{x}_b, t). \quad (12)$$

Updating the explicit particle mapping for a moving particle requires a careful reconstruction of fluid information in cells that gets uncovered in this step. We employ the approach presented in Ref. 56 which makes use of local velocity gradient information for an improved approximation.

3 | COUPLING TECHNIQUES FOR LIGHT PARTICLES

3.1 | Limitations of Current Approach

To evaluate the approach outlined in Sec. 2 for simulating a light sphere rising in a fluid, we consider the setup shown in Figure 2a, with a density ratio $\pi_p = \rho_p / \rho_f < 1$. The setup comprises a single submerged sphere of diameter d_p , initially residing at the



(a) Layout of a simulation for a rising sphere in a periodic simulation domain. The sphere rises in z direction. **(b)** Oscillations in the drag coefficient c_d at $\pi_p = 0.03$, $\text{Ga} = 170$ and $d_p = 40$.

FIGURE 2 Test case to study the stability of the coupling approach for a sphere rising inside a box.

TABLE 1 Lowest density ratios $\pi_{p,min}$ at $\text{Ga} = 100$ and a certain sphere diameter d_p for which stable results can be obtained with *MEM-LBM*-coupled LBM and particle phases.

$d_p/\Delta x$	10	15	20	30	40	50	80
$\pi_{p,min}$	0.13	0.09	0.066	0.045	0.034	0.03	0.02

bottom of the cuboidal domain with dimensions $(6.4, 6.4, 12.8)d_p$. We employ periodic boundary conditions in all directions, and set the initial position of the particle to $(3.2, 3.2, 0.6)d_p$. During the simulation, the particle rises in z direction, as characterized by the Galilei number

$$\text{Ga} = \frac{u_g d_p}{\nu_f}, \quad \text{with } u_g = \sqrt{|\pi_p - 1| g d_p}, \quad (13)$$

where g is the magnitude of the gravitational acceleration and u_g is the characteristic, gravitational velocity. In our simulations, we set $u_g = 0.01$ in lattice units and use d_p to control the overall numerical resolution. Depending on the values for π_p , Ga , and the numerical resolution, the original method can predict the upward motion of the sphere or it may fail by becoming unstable. In the latter case, we observe rapidly growing oscillations of the hydrodynamic force acting on the sphere, as illustrated in Figure 2b for an exemplary case. Here, the hydrodynamic force is expressed in terms of the dimensionless drag coefficient⁵⁷ $c_d = 2\mathbf{F}_p^{hyd} / \pi_p u_z \pi r_p^2$, where u_z is the sphere's vertical velocity and $r_p = 1/2d_p$. With increasing particle density this behavior is delayed to later stages of the simulation until completely disappearing at a certain density threshold. A simulation is considered stable, if no instabilities occurred until the rising sphere has reached its terminal ascension velocity at normalized time $t_n = t/t_g = 10$, with $t_g = d_p/u_g$.

Table 1 lists the minimum density ratio $\pi_{p,min}$ for which we observe stable results at a certain d_p for $\text{Ga} = 100$. Most notably, $\pi_{p,min}$ behaves close to inversely proportional to the sphere diameter: For instance, at a diameter of 20, 0.066 is the lowest achievable value of π_p , while at the doubled diameter (40) approximately half the density ratio (0.034) is possible to simulate. The increase in diameter entails a finer resolution of the particle-fluid interface, such that stability issues occur at smaller density ratios. However, every increase in resolution comes with a significant increase in computational costs, such that an alternative approach is required for simulating very light particles efficiently. As such, these observations establish a baseline for possible improvements.

3.2 | Analysis of the Instabilities

During each time step of our numerical method, the hydrodynamic interaction forces and torques are first applied to the particle and then a time step for the particle is executed⁴⁶. Thus, these interactions always incorporate a time lag depending on the spatial and temporal resolution. Additionally, also the liquid in the vicinity of a particle must be accelerated together with the particle. This is known as the *added mass effect*. With an explicit fluid-particle coupling, however, this effect will be accounted for with a time delay. For heavy submerged particles, the added mass effect only plays a minor role and thus does not affect the dynamics. In contrast, for very light particles, the inertial forces originate mainly from the attached fluid mass being accelerated together with the particle⁴⁵. Hence, even though the inherent inaccuracies are minor, they may lead to oscillations whose amplitude grows.

This issue becomes clear by a closer inspection of the equations that describe the temporal evolution of the linear and angular velocity of a single spherical particle submerged in fluid. In general, these equations for geometrically fully resolving simulations are given as

$$\frac{d\mathbf{u}_p}{dt} = \frac{\rho_f}{m_p} \int_S \boldsymbol{\tau} \cdot \mathbf{n} dS + \frac{(\rho_p - \rho_f)V_p}{m_p} \mathbf{g} = \frac{1}{\pi_p V_p} \int_S \boldsymbol{\tau} \cdot \mathbf{n} dS + (\pi_p - 1)\mathbf{g} = \frac{1}{\pi_p V_p} (\mathbf{F}_p^{hyd} + \mathbf{F}_p^g) \quad (14)$$

and

$$\frac{d\boldsymbol{\omega}_p}{dt} = \frac{\rho_f}{I_p} \int_S \mathbf{r} \times (\boldsymbol{\tau} \cdot \mathbf{n}) dS = \frac{1}{2/5\pi_p V_p r_p^2} \int_S \mathbf{r} \times (\boldsymbol{\tau} \cdot \mathbf{n}) dS = \frac{1}{2/5\pi_p V_p r_p^2} \mathbf{T}_p^{hyd}. \quad (15)$$

Here, $\boldsymbol{\tau}$ is the hydrodynamic stress tensor, \mathbf{n} the normal vector of the particle surface S , and \mathbf{r} the vector from the particle center to a point on its surface S ^{45,38}. For a spherical particle with radius r_p , I_p is given as $2/5m_p r_p^2$.

For very light particles, i.e. $\pi_p \rightarrow 0$, the coupling relations become singular due to a vanishing denominator in Equations (14) and (15). In other cases, a small denominator with $\pi_p \ll 1$ results in a large factor magnifying the fluid contribution.

This amplifies inaccuracies originating from the numerical computation of \mathbf{F}_p^{hyd} and \mathbf{T}_p^{hyd} in explicit fluid-particle coupling approaches⁴⁵.

3.3 | Virtual Mass Correction for the LBM

This shortcoming for simulations of light particles can be overcome by the *virtual mass approach* of Schwarz *et al.*⁴⁵. This approach has originally been developed for a classical Navier-Stokes-based solver in combination with the immersed boundary method (IBM)³⁸. The therein applied IBM originally struggled with density ratios lower than 0.4 due to oscillations in angular and translational velocities leading to a divergence within only few time steps⁴⁵. This detrimental behavior is therefore similar to the one we observed for the *MEM-LBM*-coupled simulations.

Here, we aim to employ the same stabilization technique to the LBM with the MEM-based particle coupling, following the arguments provided by Schwarz *et al.*⁴⁵ for the IBM. Alike the IBM, our numerical method accounts for the same Equations (14) and (15). Following Schwarz *et al.*⁴⁵, we introduce the concept of a virtual force

$$\mathbf{F}_p^v = m_p^v \frac{d\mathbf{u}_p}{dt}. \quad (16)$$

It uses the virtual mass $m_p^v = C_v \rho_f V_p$, which introduces the virtual mass coefficient $C_v > 0$. Adding the virtual force \mathbf{F}_p^v to both sides of Equation (14) and rearranging yields

$$\frac{d\mathbf{u}_p}{dt} = \frac{1}{(C_v + \pi_p)V_p} \int_S \boldsymbol{\tau} \cdot \mathbf{n} dS + \frac{\pi_p - 1}{C_v + \pi_p} \mathbf{g} + \frac{C_v}{C_v + \pi_p} \frac{d\mathbf{u}_p}{dt}. \quad (17)$$

A direct comparison with Equation (17) reveals, that this corresponds to a particle with altered mass $m_p + m_p^v$ onto which an additional force \mathbf{F}_p^v is acting that exactly compensates the effect of the increased mass. We explicitly note that this virtual force is different from the added mass force, a physically observable effect which is already accounted for in the geometrically fully-resolved simulation model, as we employ it here. The virtual mass coefficient C_v may be determined on an empirical basis. To attain a positive effect, C_v has to be large enough depending on the density ratio. For spherical particles, Schwarz *et al.* propose to use $C_v = 0.5$ referring to the added mass coefficient of submerged spheres⁴⁵. In our case, values of 0.5 or 1 were found to be suitable, which also satisfy the condition of a lower limit recently reported by Tavanashad *et al.*⁵⁸.

In Equation (17) the derivative of the translational particle velocity appears on either side of the equation. Physically, this is well justified, as the effect induced by the virtual mass should be exactly suppressed by the counteracting force. From an algorithmic perspective, this prevents an explicit temporal integration. As the acceleration in the current time step is to be computed and thus unknown, the acceleration on the right hand side must be approximated to allow explicit integration. Schwarz *et al.* employ second order Lagrange interpolation using the three most recent velocities in order to extrapolate the acceleration⁴⁵. Here, we alternatively propose to use the particle's acceleration from the previous time step as computed during the Velocity Verlet procedure (Section 2.2). This essentially simplifies the scheme, reduces memory consumption, and showed the most promising results in our prestudies. Denoting the previous translational acceleration as $\mathbf{a}_{p,t-1}$ then leads to

$$\frac{d\mathbf{u}_p}{dt} \approx \frac{1}{(C_v + \pi_p)V_p} \int_S \boldsymbol{\tau} \cdot \mathbf{n} dS + \frac{\pi_p - 1}{C_v + \pi_p} \mathbf{g} + \frac{C_v}{C_v + \pi_p} \mathbf{a}_{p,t-1}. \quad (18)$$

Similarly, the equation for angular motion Equation (15) is complemented with a virtual torque

$$\mathbf{T}_p^v = 2/5 C_{v,\omega} \rho_f V_p r_p^2 \frac{d\boldsymbol{\omega}_p}{dt}, \quad (19)$$

where the coefficient $C_{v,\omega}$ serves the same purpose as C_v for the translational component. Substituting the angular acceleration on the right hand side for an estimate $\boldsymbol{\beta}_{p,t-1}$ and rearranging gives

$$\frac{d\boldsymbol{\omega}_p}{dt} \approx \frac{1}{2/5 V_p r_p^2 (C_{v,\omega} + \pi_p)} \int_S \mathbf{r} \times (\boldsymbol{\tau} \cdot \mathbf{n}) dS + \frac{C_{v,\omega}}{C_{v,\omega} + \pi_p} \boldsymbol{\beta}_{p,t-1}. \quad (20)$$

Consequently, Equations (7a) and (7c) now contain \mathbf{F}_p^v and \mathbf{T}_p^v , such that $\mathbf{F}_p = \mathbf{F}_p^{hyd} + \mathbf{F}_p^g + \mathbf{F}_p^v$ and $\mathbf{T}_p = \mathbf{T}_p^{hyd} + \mathbf{T}_p^v$. The therein applied mass and moment of inertia are now given by $m_p = (\rho_p + C_v \rho_f) V_p$ and $I_p = 2/5 (\rho_p + C_{v,\omega} \rho_f) V_p r_p^2$, respectively.

Finally, Algorithm 1 outlines the complete simulation algorithm, featuring the steps introduced by the virtual mass correction in green. The update of the flow field via LBM, and the successive computation of the hydrodynamic interactions remains untouched, as well as the computation of the submerged weight force. Then, the virtual force and torque are computed based on

the translational and rotational accelerations of the previous time step. The integrator of the particle is supplied with the virtually increased mass to update the particle's position and velocities. For the remainder of the paper, we will refer to this approach as *VM-MEM-LBM*, in contrast to the original *MEM-LBM* from Section 2 that does not apply the green parts.

Algorithm 1 Outline of *VM-MEM-LBM* for a single submerged particle.

- 1: **for** each simulation step **do**
 - 2: Perform LBM step.
 - 3: Compute hydrodynamic interactions, and average over two time steps.
 - 4: Set buoyant and gravitational force.
 - 5: Calculate virtual force and torque.
 - 6: Update particle's translational and angular velocity with virtually increased mass.
 - 7: Update the particle mapping into the fluid domain.
 - 8: **end for**
-

3.4 | Validation

For validating the translational and angular components of the virtual mass approach, two different scenarios are applied next. For moderate density ratios the unchanged *MEM-LBM*, Section 2, is used as a reference, together with results from Ref. 45 where similar validation setups were used.

3.4.1 | Virtual Added Mass Force

To validate Equation (18), we employ the same setup and parameterization as described in Section 3.1. A first set of simulations are carried out with Galileo number $\text{Ga} = 100$ at density ratios $\pi_p \in \{0.1, 1.1\}$ and a resolution of $d_p = 40$, where the *MEM-LBM* serves as a reference. A final test run at $\pi_p = 0.001$, which is well below the minimal density ratio for which we expect stable simulations using *MEM-LBM* and a sphere diameter of 40 cells, employs a Galileo number of 170 and reference data is extracted from Ref. 45. For *VM-MEM-LBM*, we use $C_v = 1$ in all cases.

The normalized ascension velocity of the particle is given as $u_{z,n} = u_z/u_g$. Its mean squared error $\bar{\epsilon}_{sq}$ and mean relative error $\bar{\epsilon}_{rel}$ with respect to a reference $\hat{u}_{z,n}$ evaluated at m points in time are defined as

$$\bar{\epsilon}_{sq} = \frac{1}{m} \sum_i^m (u_{z,n,i} - \hat{u}_{z,n,i})^2, \quad (21)$$

$$\bar{\epsilon}_{rel} = \frac{1}{m} \sum_i^m \frac{u_{z,n,i} - \hat{u}_{z,n,i}}{\hat{u}_{z,n,i}}. \quad (22)$$

Additionally, the relative error in the terminal velocity is given as $\epsilon_{term,rel} = (u_{z,n,term} - \hat{u}_{z,n,term}) / \hat{u}_{z,n,term}$.

In Figure 3(a), the particle velocities of the simulations employing the *VM-MEM-LBM* are compared with their reference. Overall, all density ratios show very good agreement during the whole simulation. Yet, $\pi_p = 0.001$ deviates slightly from the reference after $t_n \approx 2$. The magnified view of the terminal velocities in Figure 3(b) shows light particles exhibiting an oscillating behavior with small amplitude of less than 0.1% of $u_{z,n}$. For heavier particles, these oscillations cannot be observed.

Visible in Table 2, across all density ratios the *VM-MEM-LBM* performs very well when compared with reference data. The mean relative errors $\bar{\epsilon}_{rel}$ amount to less than $0.3 \cdot 10^{-3}$ for all cases with a density ratio $\pi_p \geq 0.1$ (Table 2). However, the mean squared error is much larger in the comparison of the simulation at $\pi_p = 0.1$. This results from fluctuations in the velocities, observable in Figure 3. In the terminal velocity, the relative error $\epsilon_{term,rel}$ for the three larger density ratios again is almost nonexistent, listed in Table 2. At an increased terminal deviation of $\epsilon_{term,rel} = 4.64 \cdot 10^{-3}$, the error of the simulation with density ratio $\pi_p = 0.001$ is still within reasonable bounds.

Schwarz *et al.* initially report a relative error in the particle velocity of approximately 2% for their general scheme⁴⁵. After adjusting the forcing point positions of the particle-fluid-coupling in their simulations they achieve a lower error of $2 \cdot 10^{-3}$, similar to our results.

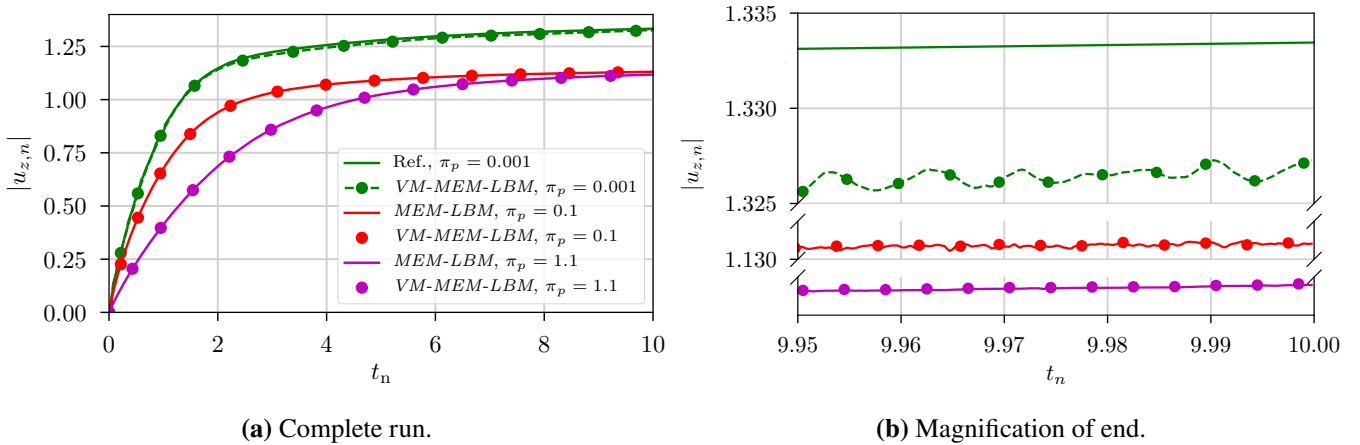


FIGURE 3 Normalized rising velocities for the validation runs using *VM-MEM-LBM* compared with their references. In case of $\pi_p = 0.001$, reference data is extracted from Ref. 45. For density ratios > 0.001 , the *MEM-LBM* served as base line.

TABLE 2 Resulting particle Reynolds number $Re_p = u_{z,term}d_p/\nu$ and errors in the normalized translational velocity $|u_n|$ when comparing the VM-MEM with reference data. Mean squared error $\bar{\epsilon}_{sq}$ and mean and terminal errors ($\bar{\epsilon}_{rel}$ and $\epsilon_{term,rel}$, respectively) relative to the reference velocities.

π_p	0.001	0.1	1.1
Ga	170	100	100
Re_p	225.64	113.08	111.77
$\bar{\epsilon}_{sq}$	$0.01 \cdot 10^{-3}$	$15.48 \cdot 10^{-9}$	$1.85 \cdot 10^{-9}$
$\bar{\epsilon}_{rel}$	$0.86 \cdot 10^{-3}$	$0.28 \cdot 10^{-3}$	$0.15 \cdot 10^{-3}$
$\epsilon_{term,rel}$	$4.64 \cdot 10^{-3}$	$0.04 \cdot 10^{-3}$	$0.06 \cdot 10^{-3}$

3.4.2 | Virtual Added Mass Torque

Similar to Ref. 45, this test case features a domain of size $(12.8, 6.4, 4.8)d_p$, confined by two walls in z direction and periodic otherwise. A sphere of 40 cells in diameter is positioned in the domain center $(6.4, 3.2, 2.4)d_p$. Here, the sphere is kept fixed at its initial position and all degrees of freedom are blocked at first. The fluid is initialized with a Couette profile, which is further driven by the upper moving wall at a constant velocity $u_w = 0.1$ in x direction during the simulation. This induces an angular momentum onto the particle, as sketched in Figure 4a. After the flow field has fully developed, rotation of the particle is allowed and its rotational velocity over time is monitored.

The setup is defined by the density ratio π_p and the particle Reynolds number $Re_p = u_p d_p / \nu$, where u_p is the undisturbed fluid velocity at the sphere's position. Since the sphere resides in the center of the domain, the fluid velocity evaluates to $u_p = 1/2u_w$. The Reynolds number $Re_p = 110$ is chosen to approximately match the situation in the force validation study in Section 3.4.1. For $\pi_p \in \{0.1, 1.1\}$, we again compare the results to *MEM-LBM*. Additionally, $\pi_p = 0.001$ is tested to check stability of *VM-MEM-LBM* in contrast to the, for this case, unstable *MEM-LBM*. We define $t_c = d_p/u_p$ and $\omega_c = u_p/d_p$ to normalize the time scale and the angular velocity, resulting in $t_n = t/t_c$ and $\omega_n = \omega_y/\omega_c$, respectively.

As displayed in Figure 4b, simulations that employ the virtual mass correction agree very well to the reference data. The mean relative errors are below $0.5 \cdot 10^{-3}$ for both cases, see Table 3. We point out that the terminal angular velocities match almost exactly. The proof-of-concept simulation at density ratio 0.001 also appears to have performed well, with a plausible trend in angular velocity and, as expected, a stronger angular acceleration than the heavier spheres.

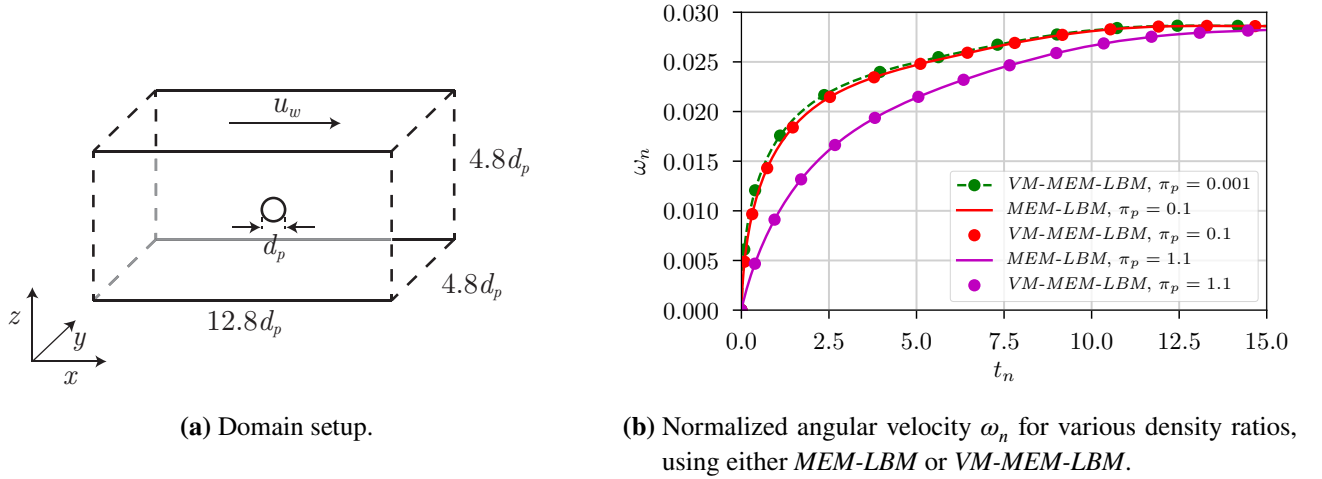


FIGURE 4 Test case (4a) and error (4b) to validate the *VM-MEM-LBM* with respect to rotation. While the sphere’s position is fixed throughout the simulation, the upper wall moving with velocity u_w drives the Couette-initialized fluid, rotating the sphere after free rotation is unblocked.

TABLE 3 Errors in the normalized angular velocity ω_n for *VM-MEM-LBM* compared to simulations using *MEM-LBM*.

π_p	0.1	1.1
$\bar{\epsilon}_{rel}$	$0.46 \cdot 10^{-3}$	$0.15 \cdot 10^{-3}$
$\epsilon_{term,rel}$	$0.01 \cdot 10^{-3}$	$0.0 \cdot 10^{-3}$

3.5 | Discussion

We have demonstrated that the virtual mass corrections can be successfully adapted to the momentum exchange method. Thus, the originally observed oscillations in the motion of very light particles are effectively reduced and stable simulations are obtained. As the *VM-MEM-LBM* relies on an approximation of the particle’s acceleration, the introduction of a certain error in comparison to *MEM-LBM* is unavoidable, as also observed in Ref. 45. The validation scenarios reveal that this error is very small: In the rising particle setup of Section 3.4.1 the error stays below 0.5%, for the cases with $\pi_p \geq 0.1$ well below that. Evaluating the accuracy of angular motion in Section 3.4.2, the error thresholds for density ratios $\pi_p \in \{0.1, 1.1\}$ are similarly low at 0.05%, at most. Nevertheless, even though the virtual mass was introduced as a solely numerically stabilizing technique for explicit fluid-particle coupling schemes, the *VM-MEM-LBM* might alter the physical results of the simulation. In phases with high acceleration changes, it artificially increases inertia by relying on the past acceleration value. Thus, for those phases, where the virtual force approximation might affect the accuracy negatively, choosing a rather low value of C_v is advisable. In all our cases, values of 0.5 or 1 were found to be sufficient. These arguments will be revisited in Section 5, where the *VM-MEM-LBM* again serves to simulate a sphere at $\pi_p = 0.001$ and results are compared to literature.

In a recent work, Tavanashad et al.⁵⁸ discussed the constant C_v more extensively and established a lower positive limit for C_v , depending on the density ratio and the added mass coefficient. Our choice of C_v is in line with this limit.

4 | ADAPTIVE GRID REFINEMENT

Accurate numerical studies of particle rising in a fluid, as they will be carried out in Section 5, require large computational domains to reduce the influence of the boundary conditions on the trajectories. On the other hand, ensuring an adequate representation of boundary layers along the particle’s surface and of the vortex structures necessitates a fine numerical resolution in those regions. Using a uniform grid for such simulations would result in enormous computational costs and limit the parameter space that can be explored substantially. To alleviate this problem, we apply adaptive grid refinement in this work which

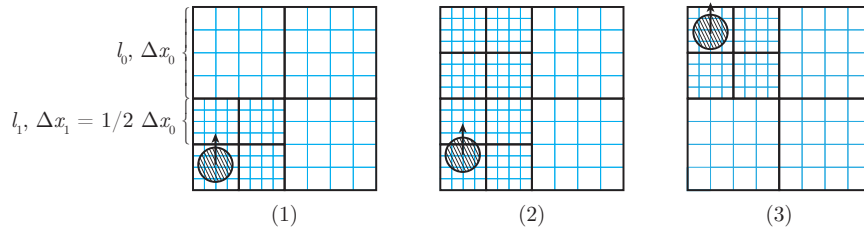


FIGURE 5 Refinement depending on the presence of a particle. Blocks are outlined black, containing 4×4 cells (outlined blue). (1) In the beginning, the block hosting the particle and its direct neighbors are on the finest level. (2) As soon as the particle enters the next block in vertical direction, the upper left non-refined block notices its presence in one of its lower neighbors and refines. (3) The particle now is fully contained within the upper quarter of the domain, such that the formerly four fine blocks at the bottom all are available to coarsen to one block. The frequency of the refinement evaluations has to be high enough to catch those particle movements, such that it always resides on the finest grid.

significantly reduces the required computational resources. In this section, we briefly outline and validate the grid refinement technique. The method makes use of the domain partitioning functionalities provided by the WALBERLA framework^{59,32}.

4.1 | Block-structured Grid Refinement with LBM

Using a block-structured domain partitioning, the computational domain is split into so-called blocks, each containing a lattice of uniformly sized cells³². Grid refinement is then carried out by uniformly dividing a block into eight smaller blocks, if needed. A block on the coarsest refinement level then has level $l = 0$, while blocks on the finest level have level $l = l_{max}$. As each block features the same number of cells, the grid spacing Δx_l of a block gets smaller with increasing level according to $\Delta x_{l+1} = 1/2 \Delta x_l$. Overall, a 2:1 balance between the blocks is maintained, meaning that the refinement level of neighboring blocks must at most differ by one.

A lattice Boltzmann method, capable of dealing with such non-uniform grids, was proposed by Rhode *et al.*⁶⁰ and is applied here. Details about its efficient implementation can be found in Refs. 59,61.

4.2 | Refinement Criteria

The refinement structure is defined by the individual target level of each block. Criteria determining the target level are presented below. They are checked regularly throughout the simulation and their result is combined to satisfy all consistency requirements. Subsequently, if some blocks are found to be on an unsuitable level of refinement, the grid is adapted by either coarsening or refining the blocks, obeying the 2:1 restriction.

4.2.1 | Particle-based Refinement Criteria

During the simulation, we ensure that blocks that are in the vicinity of particles are always on the finest grid. This is motivated by both algorithmic and physical reasons. From an algorithmic perspective, we avoid the software complexity of maintaining a consistent particle mapping across different refinement levels. At the same time, this refinement rule ensures that the finest resolution is used to resolve the boundary layer around the particle. In these regions high velocity gradients occur and are thus resolved with maximal resolution.

Alternatively, in a block where no particle is nearby, the refinement level would be allowed to become coarser. Here other refinement criteria apply combined with the 2:1 balance between neighboring blocks. A typical scenario is illustrated in Figure 5.

4.2.2 | Flow Structure-based Refinement Criteria

Secondly, special algorithmic *sensors* are applied to the fluid to compute criteria for the refinement of a block. In our case, ϕ_c , the scaled curl of the velocity field, is evaluated to detect shear layers and to control the resolution of high velocity gradients^{62,63,64}:

$$\phi_c = |\nabla \times \mathbf{u}_f| s^{(r+1)/r}. \quad (23)$$

Here, \mathbf{u}_f denotes the cell local fluid velocity, s a characteristic length scale for a cell and r a weighting coefficient. Multiplying by the weighted length scale $s^{(r+1)/r}$ facilitates the detection of weaker features in a coarser grid area, allowing weaker features to be refined when the stronger ones have been resolved⁶⁵. The length scale s can be chosen as $\sqrt[3]{V_{cell}}$ with V_{cell} as the volume of a cell or, for cubical cells, simply Δx . The constant r is commonly assigned a value of $2^{62,63,64}$. A user-defined threshold σ_c enables the adaptive manner of the fluid phase. Refinement is triggered when $\phi_c > \sigma_c$, while coarsening when $\phi_c < c\sigma_c$. To avoid repetitive refinement and coarsening, the value of c should be lower than $1/2^{(r+1)/r}$, i.e. $c \lesssim 0.35$ for $r = 2^{63}$.

4.3 | Validation

To evaluate the accuracy and performance, we compare adaptive grid refinement against a simulation using a uniform grid. The parameters are chosen to reflect a typical setup as used in the next section. In particular, we use the Galileo number $Ga = 300$ and a density ratio of 0.5 for a sphere of diameter $d_p = 100$. These properties do not require the application of *VM-MEM-LBM* to stably couple solid and fluid phases, such that the *MEM-LBM* is employed. The domain is fully periodic and of size $(7.68, 7.68, 53.76)d_p$. The sphere is positioned initially at $(3.84, 3.84, 0.6)d_p$. Starting from this point, the sphere rises up to and reaches $z_n = z/d_p = 50$ at time $t_n = 36$. In that time span we can observe the beginning of a zig-zagging motion as depicted in Figure 7. Based on this scenario, we validate the sphere's trajectory in an adaptively refining grid against the one in a fully resolved reference simulation.

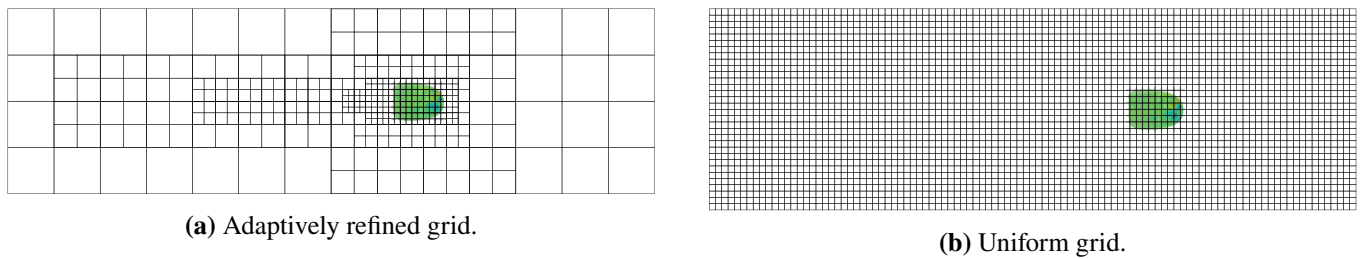


FIGURE 6 Domain partitioning at $t_n \approx 12.5$ in the adaptive and uniform case. The black lines depict the outline of the blocks. Only the lower region of the simulation domain is shown, where the primary movement direction (z) of the sphere is from left to right. The vortices around the particle are visualized using the Q criterion⁶⁶.

In the adaptively refined scenario, we set the refinement threshold σ_c to 0.001 and the coarsening factor c to 0.2. According to those values, a block is assigned one of 6 possible levels of refinement. A visual comparison of the resulting domain partitioning for a small part of the domain is provided in Figure 6a, which shows the outline of the blocks, each containing 24^3 cells. The flow field around the rising sphere is visualized by the Q criterion⁶⁶ for a time step right before the zig-zagging motion begins.

As the results show in Figure 7, the adaptively refined simulation behaves in the same manner as the one using a uniform grid after the initial trigger of the horizontal motion appears at a slight delay. The particle trajectory resides in a vertical plane, which is rotated by 45° in the horizontal plane. Figure 7a shows the normalized vertical over the horizontal sphere displacement.

By defining a time t_o at which the horizontal sphere velocity deviates from 0 and thus marks the beginning of the path-instability, we obtain a delay of $\Delta t_n = t_o^{uniform} - t_o^{refined} \approx 0.75$. This observed delay is attributed to the unpredictable and to a certain degree random appearance of the path-instability. By accounting for this delay while plotting the velocity in Figure 7c, the two lines essentially collapse into a single one. A mean relative error between the aligned velocities of 1.1% further underlines the agreement between both simulations and shows that the adaptive resolution introduces no substantial error in predicting the zig-zagging trajectory of the particle.

Regarding the computational resources of both simulations, the respective setup is described in Tab. 4 and was run on the SuperMUC-NG supercomputer at LRZ in Garching. Besides the reduction of the number of cells, the LBM for non-uniform grids carries out less time steps on coarser grids⁶⁰ which further increases the efficiency of the grid refinement approach. We find that the adaptively refined grid scenario reduced the required total core hours by a factor of 71. In our case, we thus could obtain the essentially same results in less time and using significantly less processes.

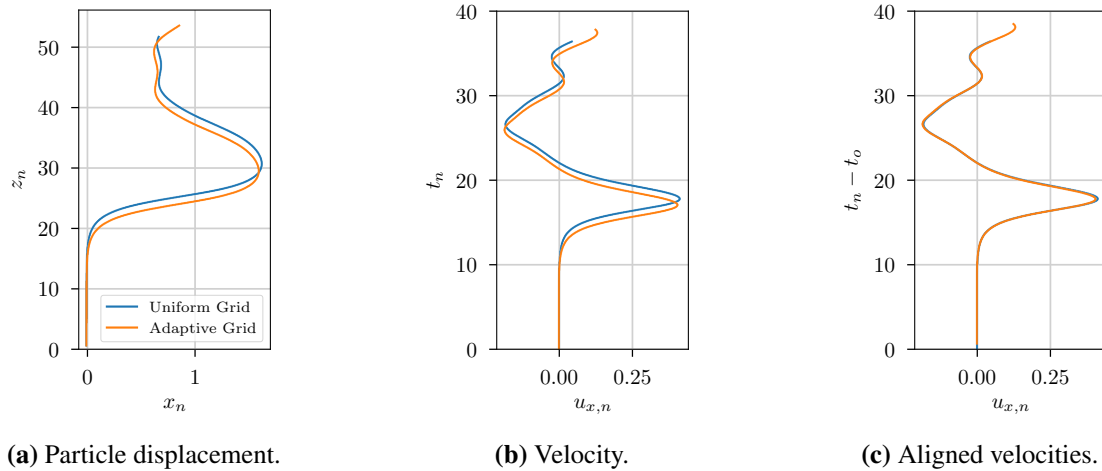


FIGURE 7 Comparison of particle trajectory and velocity for adaptively refined (orange) and uniform (blue) simulation at $Ga = 300$ and $\pi_p = 0.5$. Coordinates are normalized by particle diameter d_p , velocities by u_g .

TABLE 4 Comparison of setup and computational costs of the uniform and grid refinement scenario.

Grid	(avg.) #cells	(avg.) #blocks	#processes	run time (hours)	total core hours
Uniform	$3.06 \cdot 10^9$	221184	36864	10.27	378474
Adaptive	$3.78 \cdot 10^7$	2738.74	768	6.58	5337

As such, we have demonstrated that the here proposed grid refinement approach is capable of drastically reducing the computational costs of such a simulation while maintaining the accuracy of the uniform grid. In combination with the virtual mass correction, this enables efficient simulations of rising particles with very small density ratios.

5 | NUMERICAL STUDY OF RISING PARTICLES

The trajectories of light ascending particles have attracted growing interest since they may exhibit different regimes depending on certain parameters¹⁷. With increasing computational power, also numerical simulations became possible^{67,15,16,19,20}. In their work from 2004, Jenny, Dušek & Bouchet¹⁵ showed that the type of trajectory is mainly determined by two parameters, the density ratio π_p and the Galilei number Ga , which describes the ratio of buoyant and viscous effects. They used numerical simulation to examine the particle paths that are encountered when varying $\pi_p \in [0, 10]$ and $Ga \in [150, 350]$. In their work, they solve the Navier-Stokes equation based on a spectral-element spatial discretization in a cylindrical domain moving with the sphere. In particular, Jenny *et al.* isolated several regions in the parameter space, where rising spheres would show complex movements. The possible regimes range from steady vertical to three-dimensional chaotic, with an oblique and oblique zig-zagging regime in between.

Horowitz & Williamson¹⁷ performed a comprehensive experimental study across a wide range of sphere densities and Reynolds numbers. Most notably, they identified a “critical mass” ratio, which marked the transition between a steady rise (for a sphere with a density ratio bigger than the critical value) and zig-zagging for a certain Reynolds number beyond the one corresponding to the loss of axisymmetry in the wake. The critical mass ratio amounted to 0.36 ± 0.03 for $Re \in [260, 1550]$ and to 0.61 for Reynolds numbers higher than 1550.

More recently, Auguste & Magnaudet carried out an extensive set of simulations using a spectral element method on a moving grid²⁰ leading to results illustrated here in Figure 8. Plotting the density ratio against the Galilei number, various patterns of motion emerge with increasing Ga and varying π_p . Initially they encounter a steady vertical (SV) regime. With further increasing Galilei numbers, steady oblique (SO) and periodic oblique (PO) motion follow. Planar zig-zagging (ZZ) arises next, where

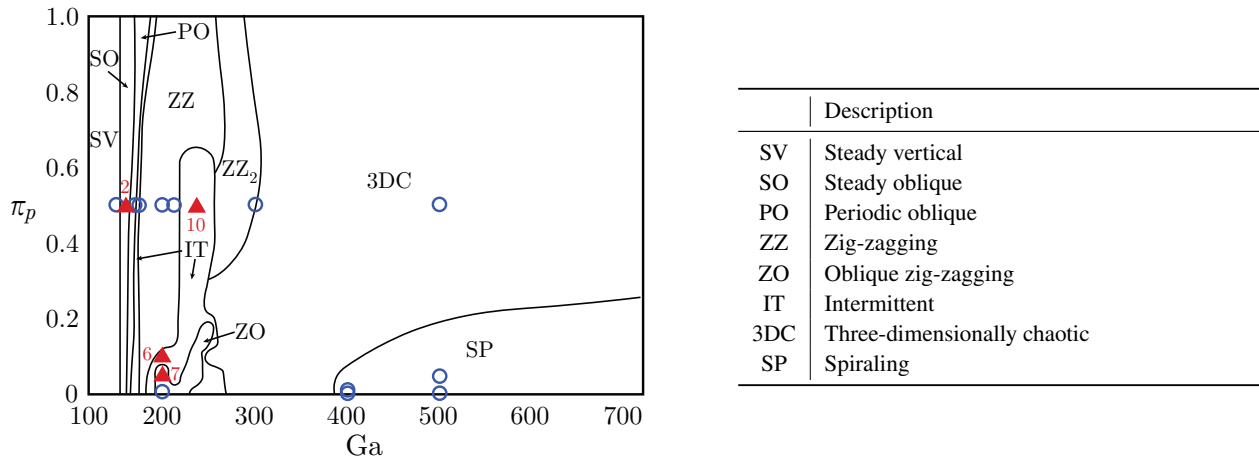


FIGURE 8 Regimes of particle motion characterized by density ratio π_p and Galilei number Ga according to Ref. 20. Overlaid points correspond to our simulations. Numbered triangles mark simulations at least partly differing from Auguste & Magnaudet’s results, circles largely confirm those.

during each change of direction and between two crests vortices are shed. Depending on the density ratio, this regime reportedly persists up to $Ga \approx 250$ for $\pi_p \gtrsim 0.6$ and only up to $Ga \approx 220$ for $0.15 \lesssim \pi_p \lesssim 0.6$. Small amplitude zig-zags for spheres with density ratio of $\gtrsim 0.6$ in a three dimensional regime termed ZZ_2 follow next; at lower density ratios an intermittent regime (IT) up to $Ga \approx 250$ occurs first. In a small stride of the map, very light spheres perform oblique zig-zagging (ZO). After a threshold value of $Ga \approx 250$ to 300, three dimensional chaotic (3DC) paths are assumed by submerged spheres of all density ratios. Beyond $Ga \approx 400$ however, some regularity is regained in the spiraling motion (SP) for very light spheres.

Except for some differences at $Ga = 200$ to 250, these findings agree largely with the ones from Zhou & Dušek¹⁹, who used a similar numerical method. On the other hand, these numerical results show deviations from the experimental studies of Horowitz & Williamson, who e.g. do not record sphere trajectories pertaining to the 3DC regime.

In the present work, we study 16 combinations of Ga and π_p that we simulate with the new method as proposed in this article, if required. This allows us to further validate our method on the one hand, and to investigate the parameter spaces where existing studies report mismatching results. The analyzed parameter combinations are marked in Figure 8.

5.1 | Simulation Setup

All simulations are performed in a cuboidal simulation domain with periodic boundary conditions in all directions. Large enough domains are chosen to avoid that turbulent structures spread so far that they would influence the particle wake or the trajectory by re-entering on the opposite side of the domain. Depending on the combination of Ga and π_p , the sphere is resolved using a varying number of cells per diameter, expressed by $d_p/\Delta x$, to assure a fine enough resolution of the boundary layer along the sphere surface and the wake³⁵. We adjust the parameter Λ_b of the MRT collision operator as introduced in Section 2.1 to $\Lambda_b = 1$, which recovers the TRT collision operator.

In all cases, adaptive grid refinement, as described in Section 4, is applied to reduce the computational cost. Depending on the domain size, 8 or 9 levels of refinement are applied. The necessity for an adaption of the grid is evaluated every 4 to 8 time steps on the coarsest grid level. The flow-based refinement criterion from Section 4.2.2 uses $\sigma_c = 0.001$ and $c = 0.2$. Similar to the simulations described in Section 3, the gravitational velocity $u_g = 0.01$ in lattice units is used which then determines the gravitational acceleration and the kinematic viscosity for the simulation. A summary of the domain size, d_p and refinement levels for each of the setups is presented in Table 5. The virtual mass approach from Section 3 in the fluid-solid coupling is only employed when it is required for stable simulations. In the present cases, this is in settings where the particle density $\pi_p = 0.001$. Then, the virtual mass coefficients are chosen as $C_v = C_{v,\omega} = 0.5$.

TABLE 5 Domain properties and sphere resolution $d_p/\Delta x$ used for the simulations of this chapter. Refinement check frequency is expressed in terms of time steps on the coarsest grid level.

Setup	Domain Size	$d_p/\Delta x$	Refinement Levels	Refinement Check Freq.
I	(38.4, 38.4, 192)	80	8	4
I _l	(38.4, 38.4, 384)	80	8	4
II	(30.72, 30.72, 215.04)	100	8	4
III	(38.4, 38.4, 307.2)	160	9	8

5.2 | Simulation Results

The 16 simulations range over of Galilei numbers from 150 to 500 at particle densities of 0.5, 0.1, 0.05, 0.01 and 0.001. The results for the key indicators are concisely summarized in Table 6. The parameters are selected such that the range of regimes from the existing literature is covered. In particular, we follow Auguste & Magnaudet’s extensive study and perform a subset of their simulations, plus two additional cases (Case 13 and 16 in Table 6).

Cases 1, 3 and 4 match with the descriptions by Auguste & Magnaudet well, pertaining to the simpler patterns of steady vertical or oblique movement. However, a disagreement is found for Case 2 where the Galilei number is specifically chosen to be located in the transition regime between SV and SO. Auguste & Magnaudet identify the SO regime here, while in our simulation the sphere appears to move SV, with visible transitions to an oblique motion.

In the next four cases, 5 to 8, we fix the Galilei number at 200, merely varying the density ratio. Here we observe three different regimes: ZZ, 3DC, and PO. While we find agreement with Auguste & Magnaudet for Cases 5 and 8, simulations 6 and 7 do not produce the PO trajectories as reported by Auguste & Magnaudet. Instead, we observe a chaotic motion of the sphere, only in Case 6 initially resembling a PO path. However, Zhou & Dušek also categorize those into the 3DC regime.

Further increasing the Galilei number and setting the density ratio to 0.5 in Cases 9 to 11 shows agreement with Auguste & Magnaudet. In addition to the already established ZZ regime in Cases 9 and 10, a second zig-zagging motion, ZZ₂, is identified in Case 11. This is characterized by a higher frequency and a smaller amplitude.

The final five scenarios feature the largest Galilei numbers. They all exhibit a spiraling motion, except Case 14. There, the trajectory loses all regularity resulting in three-dimensional chaotic motion. These findings are again in agreement with Auguste & Magnaudet. Additionally, Zhou & Dušek confirms our results in Cases 13 and 16, since our results for very light spheres (density ratio of 0.001) match their results for massless spheres.

All in all, we identify similar issues as both previous numerical studies in replicating the experiments of Horowitz & Williamson. A “critical mass ratio” and zig-zagging motion instead of three dimensional chaotic motion at increasing Reynolds numbers could not be found.

5.3 | Detailed Analysis of Results

In the following subsections, we describe our simulation results in more detail, following the analysis provided by Zhou & Dušek and Auguste & Magnaudet. This enables an in-depth comparison with these studies, based on various quantities of interest that are also provided in Table 6.

In the following, all reported particle displacements are normalized in terms of the sphere diameter d_p . As such, normalized coordinate axes corresponding to the particle’s trajectory are denoted as x_n , y_n and z_n . To quantify periodic paths, a dominant frequency f can be defined and expressed as the dimensionless Strouhal number $St = f d_p / u_{z,t}$, see Ref. 20. Here, the quasi-steady vertical velocity $u_{z,t}$ during the rise of the particle serves as reference velocity, normalized beforehand using the gravitational velocity u_g . The frequency of sphere oscillations is computed by a Fast Fourier transformation of the horizontal component of the velocity and extracting the frequency with the highest amplitude. For comparison with Zhou & Dušek, we compute the normalized frequency as $f_n = f t_g$. Further, the lateral displacement d_{cr} and height h_{cr} are determined from one typical “zig-zag” or one circle of the spiral. Inclination angles with respect to the vertical axis are computed by fitting a straight line by means of linear regression, starting at the beginning of the oblique displacement.

TABLE 6 Results for simulations of a rising sphere at various combinations of Galilei number Ga and particle density ratio π_p . For comparison, regimes as found by Auguste & Magnaudet (AM) and Zhou & Dušek (ZD) are provided next to ours. Abbreviations are explained in Figure 8. Columns labeled $u_{z,t}$, $t_{n,t}$ and $z_{n,t}$ list the normalized terminal values of the respective quantity. $d_{cr.}$ and $h_{cr.}$ describe the lateral distance and height from one crest to the following crest after completing one iteration of either a spiraling or a zig-zagging path. Regimes from literature are mostly backed by simulations in the respective case; instances, where only a visual classification by diagram is available, are marked with (*).

Case	Setup	Ga	π_p	Regime			Re	Incl. [°]	St	$d_{cr.}$	$h_{cr.}$	$u_{z,t}$	$z_{n,t}$	$t_{n,t}$
				Present	AM	ZD								
1	I	150	0.5	SV	SV	SV	196.2					1.309	191.8	147.9
2	I	162.5	0.5	SV	SO	SO	218.2					1.343	191.8	143.1
3	I	172	0.5	PO	PO	SO	232.0	4.62	0.043			1.348	191.8	144.3
4	I _l	175	0.5	PO	ZZ,PO	PO	237.0	4.74	0.042			1.350	354.5	262.6
5	II	200	0.5	ZZ	ZZ	ZZ	277.8		0.018	1.46		1.408	214.8	155.2
6	II	200	0.1	3DC	PO	3DC*	277.5					1.356	214.8	155.1
7	II	200	0.05	PO, 3DC	PO	3DC*	277.9	2.90				1.398	214.8	155.3
8	II	200	0.001	PO	PO	3DC	276.9	3.07	0.045			1.405	214.8	155.6
9	II	212.5	0.5	ZZ	ZZ	3DC	299.1		0.028	1.14		1.421	241.5	172.6
10	II	237.5	0.5	IT, ZZ	ZZ	3DC	344.5	1.34	0.098	0.22		1.449	254.9	177.9
11	II	300	0.5	ZZZ	ZZZ	3DC	447.9		0.099	0.28		1.495	238.3	162.1
12	III	400	0.01	SP	SP	3DC/SP*	591.0		0.070	0.98	14.20	1.475	171.9	117.3
13	III	400	0.001	SP	SP*	SP	586.6		0.070	1.02	14.06	1.466	294.9	201.0
14	III	500	0.5	3DC	3DC	3DC	815.2					1.600	167.2	105.0
15	III	500	0.05	SP	SP	3DC/SP*	757.3		0.067	1.08	13.81	1.510	266.3	177.6
16	III	500	0.001	SP	SP*	SP	729.3	0.20	0.074	1.09	13.22	1.455	264.8	181.0

5.3.1 | Galilei Numbers $Ga \leq 175$: Steady Vertical and Oblique

Cases 1 to 4 of Table 6 feature Setup I, covering Galilei numbers from 150 to 175 at a density ratio of 0.5. We observe steady vertical and oblique movement for these simulations.

At Galilei number 150 (Case 1), the sphere rises in a steady vertical line, with only very minor lateral displacement. This is in line with findings of both Auguste & Magnaudet and Zhou & Dušek.

Case 2 at $Ga = 162.5$ still shows movement corresponding to the SV regime. Yet for Auguste & Magnaudet, this case marked the transition to a second regime with steady oblique movement. A closer inspection of our obtained trajectory hints at a transition to obliqueness (Figure 9b), which supposedly is triggered at a slightly higher Galilei number. Unlike Case 1, the path is less oscillating around a vertical axis, but shows especially for the y direction obliqueness with lateral displacement in the order of one tenth of the sphere diameter.

Oblique paths are first observed for Case 3 at $Ga = 172$. This is the first occurrence of a PO path, and corresponds well with Auguste & Magnaudet. Further considering the inclination angle between the trajectory and the vertical axis, Auguste & Magnaudet reported an average value of approximately 4.5° , in comparison to 4.6° in our case. The comparison Strouhal number $St = 0.05$ is close to the one at hand (0.043). Figure 9c depicts the wake behind the rising particle: The sphere is constantly enclosed by a flow that builds up and sheds two axisymmetric fluid tubes in regular intervals.

The last case, 4, uses the enlarged Setup I_l to capture a longer impression of the trajectory. The general motion stays the same compared to Case 3, with the inclination slightly changing to 4.74° . Auguste & Magnaudet there noticed zig-zagging at first, which, however, ends after some iterations and changes to an oblique movement, like observed here right from the beginning.

5.3.2 | Galilei Numbers $200 \leq Ga \leq 300$: (Oblique) Zig-Zagging and Three Dimensionally Chaotic

A series of six simulations (Cases 5 to 11) using Setup II features Galilei numbers between 200 and 300 at various density ratios, as low as $\pi_p = 0.001$. Following these parametric alterations, vertical and oblique zig-zagging and three dimensionally chaotic regimes emerge.

Various trajectory types are observed at a Galilei number of 200 and three different density ratios. Planar and regular zig-zagging occurs for Case 5 at $\pi_p = 0.5$, as can be seen in Figures 10a and 11a, where the lateral displacement during each ZZ

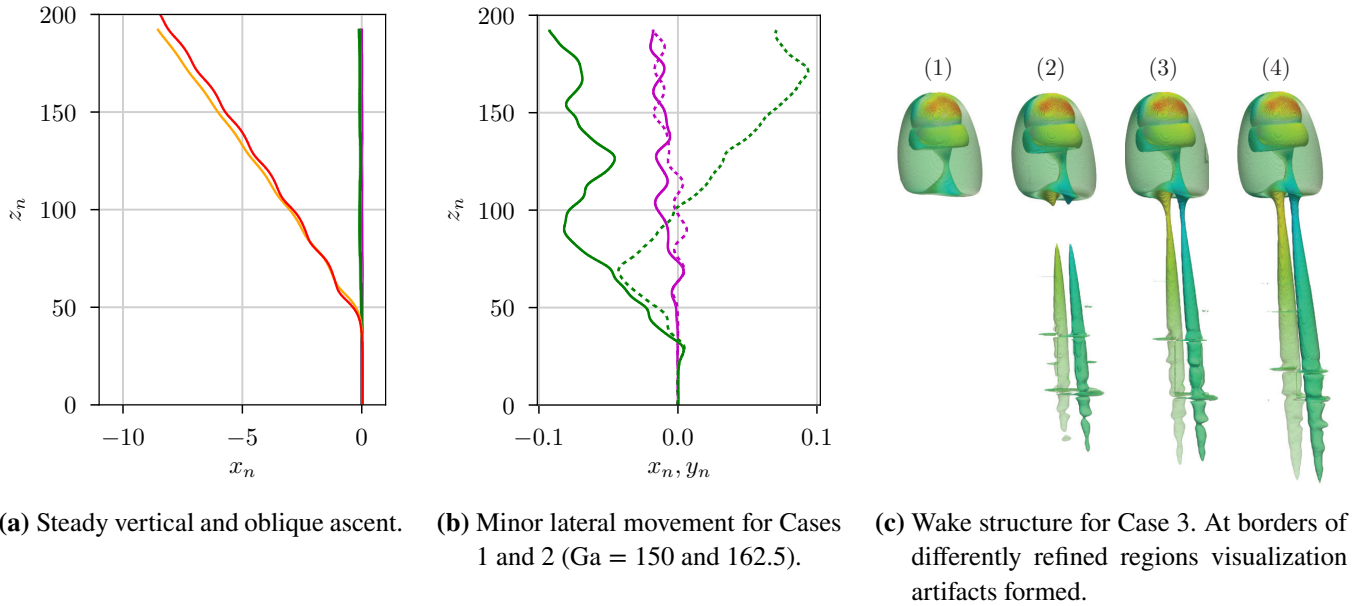


FIGURE 9 Cases 1 to 4: Plots (a, b) show trajectories at $\pi_p = 0.5$: $Ga = 150$ (magenta), 162.5 (green), 172 (orange) and 175 (red). Solid lines correspond to movement in x direction, dashed in y direction. In (c) the wake structure of Case 3 is visualized using the Q criterion at a threshold of 10^{-10} and colored by normalized vorticity (between -3.3 , blue, 0 in green and 3.8 , red).

iteration measures about $1.5d_p$. The Strouhal number is $St = 0.025$. Auguste & Magnaudet did not state detailed numbers for this set of parameters, yet depicted the corresponding path, which matches with ours in Figure 10a (blue). Zhou & Dušek more extensively reported on this case, providing a frequency spectrum of the horizontal velocity. They noticed a main peak at $f_n = 0.035$, which coincides with ours very well (0.035). The same can be stated about a second, smaller peak at $f_n = 0.10$. Furthermore, the descriptions of the particle motion correspond well.

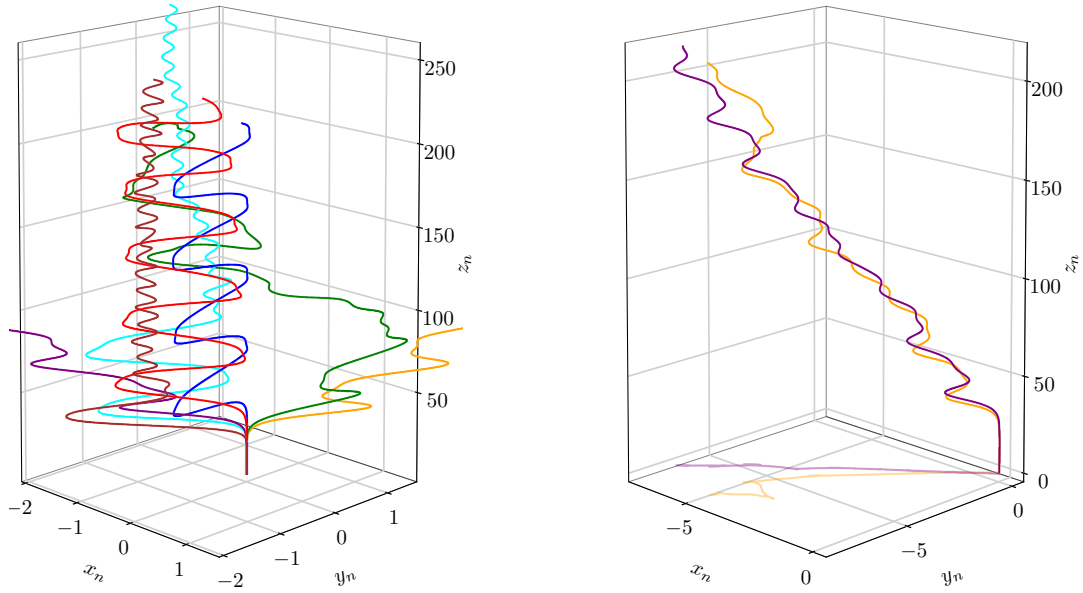
Case 6 lowers the density ratio to 0.1 , yielding an irregular zig-zagging pattern with some obliqueness up to $z_n \approx 100$ (Figure 10a). Also, three-dimensional motion up to a certain degree is observed. As such, no Strouhal number can be determined. This differs from Auguste & Magnaudet, who report periodic oblique paths here. Only the initial phase up to $z_n \approx 70$ agrees qualitatively with their simulations.

Similar observations are made for Case 7 at $\pi_p = 0.05$ in Figure 10b, which starts with a regular PO movement, continues obliquely with reduced periodicity and ends chaotic after rising up to $z_n \approx 160$. Up until that point, the average inclination of 2.9° falls within the range of $< 3^\circ$ reported by Auguste & Magnaudet.

In Case 8, a density ratio of $\pi_p = 0.001$ is simulated by utilizing the *VM-MEM-LBM*. Initially, the path resembles the one of the previous Case 7, but stays approximately planar. Additionally, its average inclination of 3° does not change much during its periodic zig-zags, such that this case can be assigned to the PO regime. As such, a Strouhal number of 0.045 for the dominant frequency ($f_n = 0.063$) can be determined. Worth mentioning is the emergence of a second not as pronounced frequency at $f_n = 0.111$ with $St = 0.079$. While Zhou & Dušek did not provide detailed results on the last three cases, their provided classification suggests chaotic movement for $Ga = 200$ and $\pi_p \leq 0.2$.

Case 9 is displayed in Figure 12, where the sphere's motion at Galilei number of 212.5 and density ratio of 0.5 behaves comparable to Case 5. It corresponds to the ZZ regime, slightly tilting its original zig-zagging plane beyond $z_n \approx 180$. The projected horizontal displacement of the zig-zagging of approximately $1.5d_p$ is also similar. Auguste & Magnaudet identified a Strouhal number ranging from 0.016 to 0.036 , confirming ours at $St \approx 0.028$.

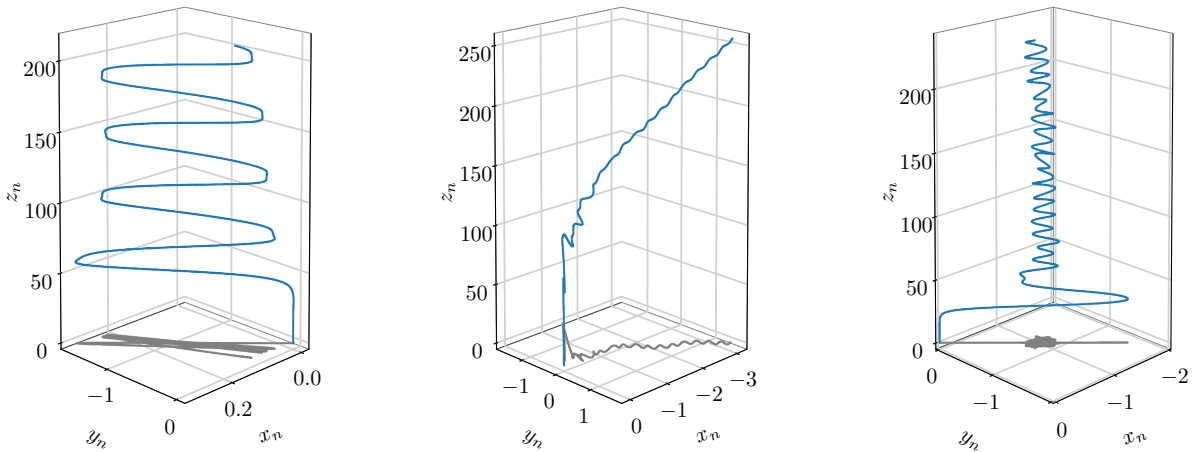
Figure 11b illustrates the trajectory of a particle at $Ga = 237.5$ and $\pi_p = 0.5$, corresponding to Case 10. The path starts as ZZ until z_n reaches 100 with a Strouhal number of $St = 0.03$, having a large amplitude. Afterwards it enters a slightly inclined plane (1.37°) with the periodic frequency increasing strongly, leading to $St \approx 0.10$. This is different from the findings of Auguste & Magnaudet, displaying a movement more prevalent for them at higher Galilei numbers between 250 and 300 . At this point, the sphere possibly already enters their ZZ₂ regime, causing a much larger Strouhal number. When considering the simulation at



(a) 3D plot of trajectories at $200 \leq Ga \leq 300$.

(b) $Ga = 200$, $\pi_p = 0.001$ (purple) and $\pi_p = 0.05$ (orange, mirrored at $(0, 0)$).

FIGURE 10 Cases 5 to 11: Trajectories for the range of Galilei numbers between 200 and 300. Combinations of Galilei number and density ratio depicted as follows. $Ga = 200$: $\pi_p = 0.5$ (blue), $\pi_p = 0.1$ (green), $\pi_p = 0.05$ (orange), $\pi_p = 0.001$ (purple); $Ga = 212.5$: $\pi_p = 0.5$ (red); $Ga = 237.5$: $\pi_p = 0.5$ (cyan); $Ga = 300$: $\pi_p = 0.5$ (brown).



(a) Case 5: $Ga = 200$, $\pi_p = 0.5$: ZZ.

(b) Case 10: $Ga = 237.5$, $\pi_p = 0.5$: ZZ and ZZ₂.

(c) Case 11: $Ga = 300$, $\pi_p = 0.5$: ZZ₂.

FIGURE 11 Cases 5, 10 and 11: Various cases of zig-zagging in their vertical and horizontal (projected to xy plane) movement.

$Ga = 240$ and $\pi_p = 0.5$ by Zhou & Dušek as reference, their results match with ours with the exception of initial large-amplitude zigzagging, as described.

ZZ₂ is also the regime in which Case 11 with a Galilei number of 300 and density ratio of 0.5 is placed. Its spatial progression is depicted in Figure 11c. Different from Auguste & Magnaudet's simulation, we observe an initial lateral swing of magnitude $2d_p$, before a more regular oscillatory path is taken. Furthermore, their Strouhal number approximately coincides with ours, at

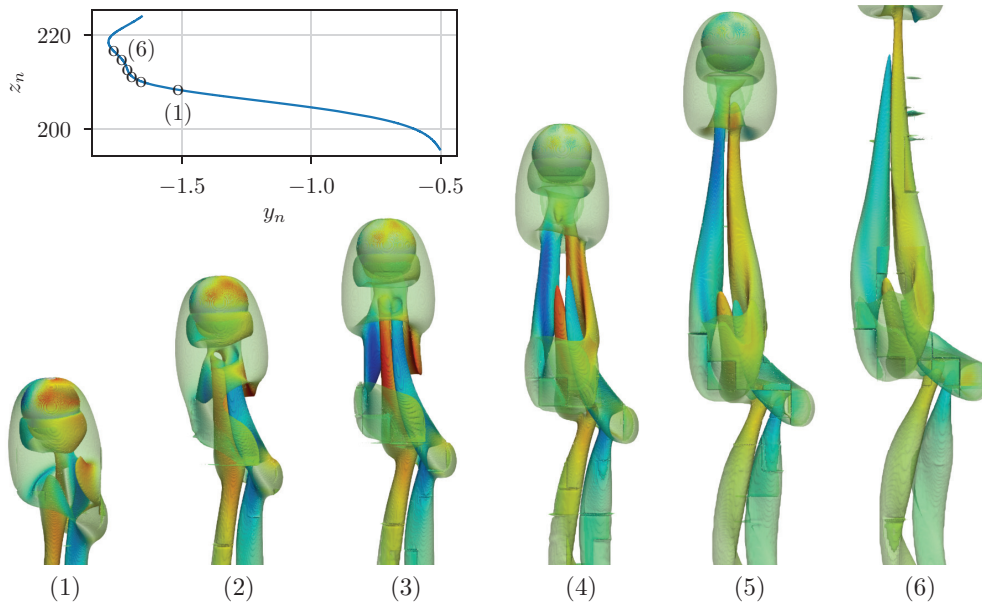
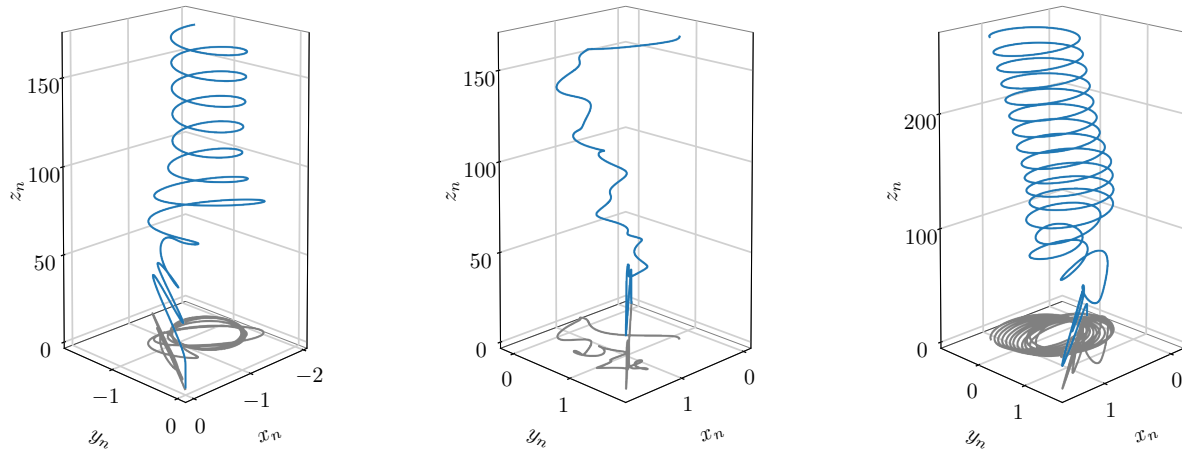


FIGURE 12 Case 9: Vortices behind a sphere of density ratio 0.5 at $Ga = 212.5$. Depicted are the states before and during movement through a crest of zig-zagging. A Q criterion threshold of 10^{-10} is employed and coloring is done by normalized vorticity, which ranges between -4 (blue) and 4 (red), green corresponding to 0.



(a) Case 12: $Ga = 400, \pi_p = 0.01$: SP. **(b)** Case 14: $Ga = 500, \pi_p = 0.5$: 3DC. **(c)** Case 16: $Ga = 500, \pi_p = 0.001$: SP.

FIGURE 13 Cases 12, 14 and 16: At $Ga = 400$ and above, two regimes are found: Three dimensional chaos (3DC) and spiraling (SP).

$St = 0.10$. The distance from crest-to-crest is $0.3d_p$, as in Auguste & Magnaudet. More so, their observation of a rotating zig-zag plane can be confirmed (see xy plot in Figure 11c). The findings of Zhou & Dušek also agree with ours.

5.3.3 | Galilei Numbers $Ga \geq 400$: Spiralling and Three Dimensionally Chaotic

The last simulations cover Galilei numbers of 400 and 500, corresponding to Cases 12 to 16. Depending on the density ratio, we encounter either chaotic movement or a highly regular spiraling regime.

This new regime is found for Case 12 at $Ga = 400$ and $\pi_p = 0.01$. The spiraling begins after an initial phase, which transforms from planar zig-zagging up until $t_n = 40$ to a three dimensional movement. After $t_n = 80$ the projection of the trajectory onto the xy plane resembles an ellipsis closely approaching the shape of a circle with a diameter of $1d_p$. The vertical stride between the spiraling iterations is approximately $14.2d_p$, resulting in $St \approx 0.07$. While not matching perfectly with Auguste & Magnaudet, these numbers come close to their spiral diameter $1.3d_p$ and Strouhal number of approximately 0.07 ($13.5d_p$ stride).

Case 13 decreases the particle density ratio further to 0.001 at $Ga = 400$ with the aid of the virtual mass approach. The vertical crest-to-crest distance changes to $14.06d_p$, while the Strouhal number stays the same. Equally, the diameter of the spiral varies only to a very minor degree. Zhou & Dušek provided results of an approximately massless sphere at this Galilei number. Its trajectories match ours, however pitch ($12.6d_p$ theirs, $14.06d_p$ ours) and terminal vertical velocity (1.382 theirs, 1.466 ours) differ to a certain degree.

Continuing with Case 14, we observe the emergence of a three dimensional chaotic region, simulated here using a Galilei number of 500 and density ratio of 0.5. This path is highly irregular and shows no sign of periodicity (Figure 13b). The occurrence of 3DC trajectories at this parameter combination was also observed by Auguste & Magnaudet and Zhou & Dušek.

Case 15 features a particle of density ratio 0.05 and Galilei number 500. Again, the particle takes up a SP path, albeit with an increased duration of the initial transition compared to the particle of Cases 12 and 13 at $Ga = 400$. Even though at $\pi_p = 0.001$, Figure 13c shows approximately the same delay as $\pi_p = 0.05$. The vertical stride of the spiral reduces slightly to $13.8d_p$ at a horizontal displacement of $1d_p$, which is reflected in an increased Strouhal number $St = 0.067$. In this instance, no reference data is available for a direct comparison. Zhou & Dušek performed two simulations at the same Galilei number and density ratios of 0.1 and 0; their depicted trajectory of $\pi_p = 0.1$ reflected the notion of the present transient from planar zig-zagging to a spiraling path. Their resulting Reynolds number of 750 confirms ours at $Re \approx 757$. After entering the quasi-steady state, the particle of Case 15 moves vertically with $u_{z,n} = 1.512$, which places close to Zhou & Dušek's at 1.406 ($\pi_p = 0$) and 1.501 ($\pi_p = 0.1$). Radius and pitch of the trajectory closely approach Zhou & Dušek's as well.

Case 16 displays a modification of the SP trajectory (Figure 13c), where the particle at $\pi_p = 0.001$ and $Ga = 500$ takes up a slightly inclined spiraling path (inclination angle $\approx 0.2^\circ$). Such behavior is also observed by Auguste & Magnaudet, who found the corresponding motion already at $\pi_p = 0.01$. The spiral is described by a diameter of $1.09d_p$ and vertical stride of $13.22d_p$; the movement along this spiral by $St = 0.074$ and $u_{z,t} = 1.455$.

6 | CONCLUSION

In this work, we present an improved LBM for simulations of light particles submerged in a fluid, including a comparison with previously established methods. This is based on a set of benchmarks that are chosen to expose specific difficulties and peculiarities arising in systems of submerged particles with density ratios $\ll 1$. In order to achieve stable simulations without excessively fine resolution, we adapt and apply the virtual mass approach of Schwarz *et al.*⁴⁵, resulting in the improved *VM-MEM-LBM*. The underlying idea is to artificially increase the mass of the particle to avoid an otherwise vanishing denominator that would amplify inaccuracies of the fluid-particle coupling scheme. This is exactly compensated by an appropriate force and torque, which in practice requires an approximation of the spheres translational and rotational acceleration. This approach is shown to enable density ratios of 0.001 and which would thus permit e.g. the simulation of spherical air bubbles in water. The numerical stabilization scheme is validated both with respect to the accuracy of rotational and translational velocities.

In order to further increase the computational efficiency of the parallel LBM code, we employ adaptive grid refinement. This ensures an adequate and accurate representation of the flow features while permitting large computational domains. Areas in need of refinement are identified by employing sensors evaluating the state of the fluid and the solid phase. The evaluation of the grid adaptation criteria is invoked at regular time intervals. For the case of a rising sphere, the computational cost could be reduced by a factor of 71, when compared to executing same simulation scenario on a uniform fine grid. This is achieved while the accuracy is essentially unaffected.

The efficiency improvement supplied by the adaptive grid refinement algorithm is finally applied in 16 distinct simulation scenarios that study the trajectories of a single rising sphere. In the cases of smallest density ratio of 0.001, the virtual mass approach proved to be essential to reach a stable time stepping. A multitude of different trajectory types is observed and the results are compared to data from the literature. This includes trajectory classes such as vertical to oblique, zig-zagging, spiraling, three dimensional chaos, and intermittent motion. In many cases good agreement to experimental and numerical studies could be found, for the broad classification via the regimes but also for specific parameters like terminal rising velocities and oscillation



FIGURE 14 Case 15: Vortices behind a sphere of density ratio 0.05 at $Ga = 500$. In frames 4 and 5 the three vortex threads delivering a constant torque to the ascending sphere are well visible. A Q criterion threshold of 10^{-10} is employed and coloring is done by normalized vorticity, which ranges between -10 (blue) and 10 (red). Lighter colors correspond to stronger magnitude.

frequencies. This served as a further validation of the here presented approach and showcased its applicability for predictions of complex particle dynamics. In some cases, the existing literature provided contradicting statements regarding the observed regime of motion and we observed supporting arguments for one or the other.

We note that while validated here for single spherical particles, our new method is neither restricted to a single particle nor to spherical shapes. The *VM-MEM-LBM* is also suitable for a wide range of physical parameters, and it can be employed in domains of arbitrary shape. This is considered a major improvement to the numerical schemes applied previously in the simulation studies of trajectories of rising particles. A massively parallel and efficient implementation is available in the open-source *WALBERLA* framework³², enabling the simulation of ensembles of several submerged particles and to study their collective motion. Such studies will be the topic of future research.

ACKNOWLEDGMENTS

The authors gratefully acknowledge the Erlangen Regional Computing Center (www.rrze.fau.de) as well as the Gauss Centre for Supercomputing e.V. (www.gauss-centre.eu) for funding this project by providing computing time on their supercomputers.

References

1. Andrady AL. Microplastics in the marine environment. *Marine Pollution Bulletin* 2011; 62(8): 1596 - 1605. doi: <https://doi.org/10.1016/j.marpolbul.2011.05.030>
2. Wright SL, Thompson RC, Galloway TS. The physical impacts of microplastics on marine organisms: a review. *Environmental pollution (Barking, Essex : 1987)* 2013; 178: 483–492. doi: 10.1016/j.envpol.2013.02.031
3. Cole M, Lindeque P, Halsband C, Galloway TS. Microplastics as contaminants in the marine environment: A review. *Marine Pollution Bulletin* 2011; 62(12): 2588–2597. doi: 10.1016/j.marpolbul.2011.09.025
4. Driedger AG, Dürr HH, Mitchell K, Van Cappellen P. Plastic debris in the Laurentian Great Lakes: A review. *Journal of Great Lakes Research* 2015; 41(1): 9–19. doi: 10.1016/j.jglr.2014.12.020
5. Thorpe SA, Hall AJ. Bubble clouds and temperature anomalies in the upper ocean. *Nature* 1988; 328(6125): 48–51. doi: 10.1038/328048a0
6. Weller RA. Not so quiet on the ocean front. *Nature* 1990; 348(6298): 199–200. doi: 10.1038/348199a0
7. Alméras E, Risso F, Roig V, Cazin S, Plais C, Augier F. Mixing by bubble-induced turbulence. *Journal of Fluid Mechanics* 2015; 776: 458–474. doi: 10.1017/jfm.2015.338
8. Mathai V, Huisman SG, Sun C, Lohse D, Bourgoïn M. Enhanced dispersion of big bubbles in turbulence. 2018(1): 1–6.
9. Mathai V, Lohse D, Sun C. Bubbly and Buoyant Particle-Laden Turbulent Flows. *Annual Review of Condensed Matter Physics* 2020; 11(1): 529–559. doi: 10.1146/annurev-conmatphys-031119-050637
10. Bourgoïn M, Xu H. Focus on dynamics of particles in turbulence. *New Journal of Physics* 2014; 16. doi: 10.1088/1367-2630/16/8/085010
11. Mathai V, Zhu X, Sun C, Lohse D. Flutter to tumble transition of buoyant spheres triggered by rotational inertia changes. *Nature Communications* 2018; 9(1): 1–7. doi: 10.1038/s41467-018-04177-w
12. Murrow H, Henry R. Self-Induced Balloon Motions. *Journal of Applied Meteorology and Climatology* 1964; 4(1): 131–138. doi: 10.1175/1520-0450(1965)004<0131:SIBM>2.0.CO;2
13. Scoggins JR. Aerodynamics of spherical balloon wind sensors. *Journal of Geophysical Research* 1964; 69(4): 591–598. doi: 10.1029/jz069i004p00591
14. Lugt H. Autorotation. *Annual Review of Fluid Mechanics* 1983; 15: 123–147. doi: 10.1146/annurev.fl.15.010183.001011
15. Jenny M, Dušek J, Bouchet G. Instabilities and transition of a sphere falling or ascending freely in a Newtonian fluid. *Journal of Fluid Mechanics* 2004; 508(508): 201–239. doi: 10.1017/S0022112004009164
16. Biesheuvel A, Veldhuis C. An experimental study of the regimes of motion of spheres falling or ascending freely in a Newtonian fluid. *International Journal of Multiphase Flow* 2007; 33(10): 1074–1087. doi: 10.1016/j.ijmultiphaseflow.2007.05.002
17. Horowitz M, Williamson CH. The effect of Reynolds number on the dynamics and wakes of freely rising and falling spheres. *Journal of Fluid Mechanics* 2010; 651: 251–294. doi: 10.1017/S0022112009993934
18. Ostmann S, Chaves H, Brücker C. Path instabilities of light particles rising in a liquid with background rotation. *Journal of Fluids and Structures* 2017; 70: 403–416. doi: 10.1016/j.jfluidstructs.2017.02.007
19. Zhou W, Dušek J. Chaotic states and order in the chaos of the paths of freely falling and ascending spheres. *International Journal of Multiphase Flow* 2015; 75: 205–223. doi: 10.1016/j.ijmultiphaseflow.2015.05.010
20. Auguste F, Magnaudet J. Path oscillations and enhanced drag of light rising spheres. *Journal of Fluid Mechanics* 2018; 841: 228–266. doi: 10.1017/jfm.2018.100

21. Versteeg HK, Malalasekera W. *An introduction to computational fluid dynamics: the finite volume method*. Pearson education . 2007.
22. F. Moukalled, L. Mangani MD. *The Finite Volume Method in Computational Fluid Dynamics*. 113. Springer . 2015.
23. Chen S, Doolen GD. Lattice Boltzmann Method for Fluid Flows. *Annual Review of Fluid Mechanics* 1998; 30(1): 329–364. doi: 10.1146/annurev.fluid.30.1.329
24. Aidun CK, Clausen JR. Lattice-boltzmann method for complex flows. *Annual Review of Fluid Mechanics* 2010; 42: 439–472. doi: 10.1146/annurev-fluid-121108-145519
25. Clift R, Grace JR, Weber M. *Bubbles, Drops, and Particles* . 1978.
26. Rettinger C, Godenschwager C, Eibl S, et al. Fully Resolved Simulations of Dune Formation in Riverbeds. In: Kunkel JM, Yokota R, Balaji P, Keyes D., eds. *High Performance Computing* Springer International Publishing; 2017; Cham: 3–21
27. Vowinckel B, Biegert E, Luzzatto-Fegiz P, Meiburg E. Consolidation of freshly deposited cohesive and noncohesive sediment: Particle-resolved simulations. *Phys. Rev. Fluids* 2019; 4: 074305. doi: 10.1103/PhysRevFluids.4.074305
28. Peng C, Ayala OM, Wang LP. A direct numerical investigation of two-way interactions in a particle-laden turbulent channel flow. *Journal of Fluid Mechanics* 2019; 875: 1096–1144. doi: 10.1017/jfm.2019.509
29. Benseghier Z, Cuéllar P, Luu LH, Bonelli S, Philippe P. A parallel GPU-based computational framework for the micromechanical analysis of geotechnical and erosion problems. *Computers and Geotechnics* 2020; 120: 103404. doi: 10.1016/j.compgeo.2019.103404
30. Götz J, Iglberger K, Feichtinger C, Donath S, Rüde U. Coupling multibody dynamics and computational fluid dynamics on 8192 processor cores. *Parallel Computing* 2010; 36(2): 142 - 151. doi: 10.1016/j.parco.2010.01.005
31. Hasert M, Masilamani K, Zimny S, et al. Complex fluid simulations with the parallel tree-based Lattice Boltzmann solver Musubi. *Journal of Computational Science* 2014; 5(5): 784 - 794. doi: 10.1016/j.jocs.2013.11.001
32. Bauer M, Eibl S, Godenschwager C, et al. WALBERLA: A block-structured high-performance framework for multiphysics simulations. *Computers and Mathematics with Applications* 2020. doi: 10.1016/j.camwa.2020.01.007
33. Ladd AJ. Numerical Simulations of Particulate Suspensions Via a Discretized Boltzmann Equation. Part 1. Theoretical Foundation. *Journal of Fluid Mechanics* 1994; 271: 285–309. doi: 10.1017/S0022112094001771
34. Aidun CK, Lu Y, Ding EJ. Direct analysis of particulate suspensions with inertia using the discrete Boltzmann equation. *Journal of Fluid Mechanics* 1998; 373: 287–311. doi: 10.1017/S0022112098002493
35. Rettinger C, Rüde U. A comparative study of fluid-particle coupling methods for fully resolved lattice Boltzmann simulations. *Computers and Fluids* 2017; 154: 74–89. doi: 10.1016/j.compfluid.2017.05.033
36. Ladd AJC. Numerical simulations of particulate suspensions via a discretized Boltzmann equation. Part 2. Numerical results. *Journal of Fluid Mechanics* 1994; 271: 311–339. doi: 10.1017/S0022112094001783
37. Uhlmann M. An immersed boundary method with direct forcing for the simulation of particulate flows. *Journal of Computational Physics* 2005; 209(2): 448–476. doi: 10.1016/j.jcp.2005.03.017
38. Kempe T, Fröhlich J. An improved immersed boundary method with direct forcing for the simulation of particle laden flows. *Journal of Computational Physics* 2012. doi: 10.1016/j.jcp.2012.01.021
39. Breugem WP. A second-order accurate immersed boundary method for fully resolved simulations of particle-laden flows. *Journal of Computational Physics* 2012; 231(13): 4469–4498. doi: 10.1016/j.jcp.2012.02.026
40. Inamuro T, Ogata T, Tajima S, Konishi N. A lattice Boltzmann method for incompressible two-phase flows with large density differences. *Journal of Computational Physics* 2004; 198(2): 628–644. doi: 10.1016/j.jcp.2004.01.019

41. Apte SV, Finn JR. A variable-density fictitious domain method for particulate flows with broad range of particle-fluid density ratios. *Journal of Computational Physics* 2013; 243: 109–129. doi: 10.1016/j.jcp.2012.12.021
42. Banks J, Henshaw W, Schwendeman D, Tang Q. A stable partitioned FSI algorithm for rigid bodies and incompressible flow in three dimensions. *Journal of Computational Physics* 2018; 373: 455–492. doi: 10.1016/j.jcp.2018.06.072
43. Jenny M, Dušek J. Efficient numerical method for the direct numerical simulation of the flow past a single light moving spherical body in transitional regimes. *Journal of Computational Physics* 2004; 194(1): 215–232. doi: 10.1016/j.jcp.2003.09.004
44. Hu HH, Patankar NA, Zhu MY. Direct Numerical Simulations of Fluid-Solid Systems Using the Arbitrary Lagrangian-Eulerian Technique. *Journal of Computational Physics* 2001; 169(2): 427–462. doi: 10.1006/jcph.2000.6592
45. Schwarz S, Kempe T, Fröhlich J. A temporal discretization scheme to compute the motion of light particles in viscous flows by an immersed boundary method. *Journal of Computational Physics* 2015; 281: 591–613. doi: 10.1016/j.jcp.2014.10.039
46. Rettinger C, Rüde U. An efficient four-way coupled lattice Boltzmann - discrete element method for fully resolved simulations of particle-laden flows. 2020: 1–37.
47. Krüger T, Kusumaatmaja H, Kuzmin A, Shardt O, Silva G, Viggien EM. *The lattice Boltzmann method*. Springer . 2017
48. Qian YH, D’Humières D, Lallemand P. Lattice bkg models for navier-stokes equation. *Epl* 1992; 17(6): 479–484. doi: 10.1209/0295-5075/17/6/001
49. He X, Luo LS. Lattice Boltzmann model for the incompressible Navier–Stokes equation. *Journal of Statistical Physics* 1997; 88(3-4): 927–944. doi: 10.1023/B:JOSS.0000015179.12689.e4
50. D’Humières D, Ginzburg I, Krafczyk M, Lallemand P, Luo LS. Multiple-relaxation-time lattice Boltzmann models in three dimensions. *Philosophical Transactions of the Royal Society A: Mathematical, Physical and Engineering Sciences* 2002; 360(1792): 437–451. doi: 10.1098/rsta.2001.0955
51. Dünweg B, Schiller UD, Ladd AJC. Statistical mechanics of the fluctuating lattice Boltzmann equation. *Phys. Rev. E* 2007; 76: 036704. doi: 10.1103/PhysRevE.76.036704
52. Ginzburg I, Verhaeghe F, D’Humières D. Two-relaxation-time Lattice Boltzmann scheme: About parametrization, velocity, pressure and mixed boundary conditions. *Communications in Computational Physics* 2008; 3(2): 427–478.
53. Khirevich S, Ginzburg I, Tallarek U. Coarse- and fine-grid numerical behavior of MRT/TRT lattice-Boltzmann schemes in regular and random sphere packings. *Journal of Computational Physics* 2015; 281: 708 - 742. doi: 10.1016/j.jcp.2014.10.038
54. Preclik T, Rüde U. Ultrascale simulations of non-smooth granular dynamics. *Computational Particle Mechanics* 2015; 2(2): 173–196. doi: 10.1007/s40571-015-0047-6
55. Wen B, Zhang C, Tu Y, Wang C, Fang H. Galilean invariant fluid-solid interfacial dynamics in lattice Boltzmann simulations. *Journal of Computational Physics* 2014; 266: 161–170. doi: 10.1016/j.jcp.2014.02.018
56. Dorschner B, Chikatamarla S, Bösch F, Karlin I. Grad’s approximation for moving and stationary walls in entropic lattice Boltzmann simulations. *Journal of Computational Physics* 2015; 295: 340 - 354. doi: 10.1016/j.jcp.2015.04.017
57. Hölzer A, Sommerfeld M. New simple correlation formula for the drag coefficient of non-spherical particles. *Powder Technology* 2008; 184(3): 361–365. doi: 10.1016/j.powtec.2007.08.021
58. Tavanashad V, Subramaniam S. Fully resolved simulation of dense suspensions of freely evolving buoyant particles using an improved immersed boundary method. *International Journal of Multiphase Flow* 2020; 132: 103396. doi: 10.1016/j.ijmultiphaseflow.2020.103396
59. Schornbaum F, Rüde U. Massively parallel algorithms for the lattice Boltzmann method on nonuniform grids. *SIAM Journal on Scientific Computing* 2016; 38(2): C96–C126. doi: 10.1137/15M1035240

60. Rohde M, Kandhai D, Derksen JJ, Akker v. dHE. A generic, mass conservative local grid refinement technique for lattice-Boltzmann schemes. *International Journal for Numerical Methods in Fluids* 2006; 51(4): 439–468. doi: 10.1002/fld.1140
61. Schornbaum F, Rde U. Extreme-scale block-structured adaptive mesh refinement. *SIAM Journal on Scientific Computing* 2018; 40(3): C358–C387. doi: 10.1137/17M1128411
62. Crouse B, Rank E, Krafczyk M, Tlke J. A LB-based approach for adaptive flow simulations. *International Journal of Modern Physics B* 2003; 17(1-2): 109–112. doi: 10.1142/s0217979203017163
63. Yuan R, Zhong C. An immersed-boundary method for compressible viscous flows and its application in the gas-kinetic BGK scheme. *Applied Mathematical Modelling* 2018; 55: 417–446. doi: 10.1016/j.apm.2017.10.003
64. Deister F, Hirschelt EH. Adaptive cartesian/prism grid generation and solutions for arbitrary geometries. *37th Aerospace Sciences Meeting and Exhibit* 1999(c). doi: 10.2514/6.1999-782
65. De Zeeuw D. *A quadtree-based adaptively-refined Cartesian-grid algorithm for solution of the Euler equations*. PhD thesis. 1993
66. Hunt J, Wray A, Moin P. Eddies, streams, and convergence zones in turbulent flows. *Center for Turbulence Research, Proceedings of the Summer Program* 1988(1970): 193–208.
67. Jenny M, Bouchet G, Dušek J. Nonvertical ascension or fall of a free sphere in a Newtonian fluid. *Physics of Fluids* 2003; 15(1): L9–L12. doi: 10.1063/1.1529179

